MEMS BASED WIRELESS SENSING AND THERAPEUTIC SYSTEMS FOR BIOMEDICAL APPLICATIONS

by

PRAVEEN PANDOJIRAO-SUNKOJIRAO

Presented to the Faculty of the Graduate School of
The University of Texas at Arlington in Partial Fulfillment
of the Requirements
for the Degree of

DOCTOR OF PHILOSOPHY

THE UNIVERSITY OF TEXAS AT ARLINGTON
December 2009

Dedicated to my parents, family and friends.

ACKNOWLEDGEMENTS

I would like to thank my supervising professor Dr. Jung-Chih Chiao for his patience, motivation, and encouragement, and also for his invaluable advice during the course of my masters and doctoral studies. I wish to thank Dr. Dereje Agonafer, Dr. Michael Vasilyev, Dr. Ronald Carter, and Dr. Venkat Devarajan for their interest in my research and for taking time to serve in my dissertation committee.

I would also like to extend my appreciation to Dr. Jian Yang, Dr. John Priest and Dr. Digant Dave for giving me access to their research laboratories. I would also like to thank the staff of Nanofabrication research and teaching facility, Dr. Fatima Amir, Dr. Eduardo Maldonado, Dennis Bueno, and Paul C. Logan for their valuable inputs during my fabrication. I would also like to thank my colleagues Smitha, Uday, Naresh, Pratibha, Paul, Sajal, and Richard for their help with my experiments. I would like to thank all the past, and current members of iMEMS for their valuable suggestions. I would like to thank all the staff of Electrical Engineering, and Sally Thompson from Mechanical and Aerospace Engineering for their help with departmental procedures. I am grateful to all the teachers who taught me during the years I spent in school, first in India and then in the United States.

Finally, I would like to express my deep gratitude to my parents, brother, sister in-law, niece and nephew who have encouraged and inspired me and supported my undergraduate and graduate studies and also for their sacrifice, encouragement and patience. I also thank several of my friends who have helped me throughout my career.

December 8, 2009

ABSTRACT

MEMS BASED WIRELESS SENSING AND THERAPEUTIC SYSTEMS FOR BIOMEDICAL APPLICATIONS

PRAVEEN PANDOJIRAO-SUNKOJIRAO, Ph.D.

The University of Texas at Arlington, 2009

Supervising Professor: Jung-Chih Chiao

Miniaturized devices *in vivo* for accurate diagnosis and prognosis in therapy to detect various physiological parameters inside human body have been a goal for efficient healthcare. In this perspective, microelectromechanical system (MEMS) devices providing small size features and new transduction functions benefit such biomedical applications. The features in MEMS devices also allow integration of CMOS circuitry and wireless communication for electronic control as well as actuation functionalities for driving mechanical parts for scanning, moving and probing. In this work, feasibility studies for two novel sensing systems: an *in vivo* optical fiber based spectral optical coherence tomography (OCT) imaging system and a passive wireless pressure sensor, having potential applications in diagnosis and therapy for gastrointestinal (GI) disorders have been proposed and demonstrated.

Spectral OCT is a noninvasive imaging system and has several advantages such as high penetration depths, cross sectional imaging and micrometer resolution into the tissues. OCT can provide virtual biopsy into the depth of the tissues and 3-D visualization of the cells. Spectral OCT provides fast scanning and high resolution for

the tissues. In our design, an improved scanner using electromagnetic actuation for fiber-based OCT systems has been demonstrated. The optical fiber provides small features allowing *in vivo* applications inside human body using conventional endoscopes. This system employs external electromagnetic actuation making it very small for *in vivo* uses without the requirement of electrical connection from outside to the scanner. Cantilevers coated with various non-magnetized ferromagnetic materials and actuated by external magnetic fields were designed and characterized to demonstrate the feasibility for remote scanning. Finite element analysis and analytic solutions were developed to design and characterize the designs of the scanner. Different magnetic materials such as cobalt, iron and nickel submicron-scale powders were used to demonstrate the actuation of the imaging systems. Magnetic materials characterized using the magnetic hysteresis curves, magnetic properties and mechanical properties were found to guide design principles for the scanner. Optical experiments were conducted for each device to verify the designs. Plastic cantilevers were coated with a mixture of 50% enamel paint and 50% various ferromagnetic materials. The dynamic measurements were performed under the external excitation of an electromagnet. Experiments with different ferromagnetic materials and different suspended cantilever lengths of 80mm, 70mm, and 60mm were performed to compare with theory. The dynamic displacements and resonant frequencies of the actuation were measured. The results presented could be used to guide designs of magnetically actuated cantilever scanners toward specific requirements in applications. Cobalt coated 80mm long cantilever had the highest scanning distance of 4.96mm while the iron coated 60mm long cantilever had the highest scanning frequency of 16.8Hz with 1mm thick coatings. Imaging feasibility on human tissue was demonstrated using a nickel coated 70mm long cantilever. A scan distance of 1.4mm was obtained with a maximum scanning frequency of 28Hz.

For GI manometry, we proposed a novel miniature, passive wireless pressure sensing system on a flexible substrate. The sensor can be incorporated with thin-film metal or biodegradable esophageal stents for therapy and prognosis. Planar variable interdigitated capacitors (IDC) were designed to measure the variations in radial pressures and strains. Encapsulation by a layer of poly-dimethylsiloxane (PDMS) of the sensors made the device elastic, deformable and biocompatible. The flexible IDC was fabricated allowing changes in capacitance due to pressure variations. Capacitance characterization using linear pull test showed that the capacitance of the IDC for a given pull distance remained constant even after repeated cycles. Force characterization showed a sensitivity 0.5pF/N. Radial pressure measurement feasibility was demonstrated using an *in vitro* system. Pressure sensitivity was found to be 0.1pf/kPa. In an integrated wireless batteryless environment, the sensitivity of the variable IDC induced frequency change was 0.14kHz/kPa. This type of sensor can be easily incorporated in commercial metal stents clinically used or a biodegradable one providing *in vivo* remote pressure measurements for GI motility. Strain tests using the IDC showed that the sensor is suitable for axial pressure measurements. The sensor can be incorporated with thin-film metal on biodegradable esophageal stents for therapy and prognosis. This allows for monitoring pressure over fixed pre-determined periods of time after which the sensor passes through the digestive system. The use of biodegradable materials thus eliminates the need for additional procedures to remove the sensor and the stent.

TABLE OF CONTENTS

LIST OF FIGURES

LIST OF TABLES

CHAPTER 1

INTRODUCTION

1.1 Motivation

The accelerated growth of new micro-electro-mechanical systems (MEMS) for biomedical instrumentation in recent years is due to the demand for higher-quality medical care and emphasis on preventive care, accuracy, and need for minimally invasive procedures [3–7]. Endoscopic techniques using fiber optic instruments and small percutaneous operating ports, rather than wide-open incisions have largely replaced traditional methods for minor procedures. The advantages of these technologies are: reduced operative time, lower risk of infection, less trauma and discomfort, shorter hospital stays, and ultimately lower cost. Minimally invasive procedures offer opportunities for therapies including targeting of specific tumors and other organs for blood delivery, microvisualization and manipulation, implantation of microsensors and microactuators and other components of a larger implanted device or external system. Recent research has focussed on the use of MEMS based devices for cancer diagnosis and therapy.

Cancer is a class of diseases in which a group of cells display uncontrolled growth (division beyond the normal limits), invasion (intrusion on and destruction of adjacent tissues), and sometimes metastasis (spread to other locations in the body via lymph nodes or blood). These three malignant properties of cancers differentiate them from benign tumors, which are self-limited, and do not invade or metastasize. Esophageal cancer is one of the deadliest cancer worldwide [8, 9]. According to The American Cancer Society:

- In 2009, more than 16,000 new esophageal cancer cases will be diagnosed and more than 14,000 deaths are estimated
- Increasing at a rate of 1% in the western countries
- Esophageal cancer is 75% to 80% more common among men than woman
- Squamous cell carcinoma is the most common type of cancer of the esophagus among African Americans, while adenocarcinoma is more common in whites
- Lifetime risk is 1 in 200 in the the United States. The squamous cell carcinoma type esophageal cancer is more common in countries like Iran, northern China, India, and southern Africa with cancer rates that are 10 to 100 times higher than in the United States
- Survival rate has improved to 10% compared to 1% in the 1960s[1]

In the last two decades, there has been a 350% increase in adenocarcinoma of the esophagus, a type of cancer that is related to the cellular changes in the esophagus which are the hallmark of Barrett's esophagus and arise from gastroesophageal reflux disease. Even though the reflux symptoms are strong indicators of the risk, there is approximately 40% chance that Barrett's esophagus occurs without any symptoms of reflux at all. According to estimates from the American Gastroenterological Association, in 2005 there were more than 3 million Americans living with Barrett's esophagus, a condition that can lead to esophageal cancer.

1.2 Specific Aims

The overall focus of this project is on the following specific aims

1. Develop and characterize an imaging system based on optical coherence tomography.

[1]These survival rates are based on 5-year relative survival rates which refers to the percent of patients who live at least 5 years after their cancer is diagnosed.

Confocal microscopy has been the gold standard for high resolution imaging within turbid media, such as tissue, but large bulky optics and expensive electronics have limited its clinical use to tertiary care centers with extensive funding and infrastructure. A fiber optic assembly integrated with a cantilever based scanning system coupled to a broadband laser source was developed to address this issue. This type of imaging system is useful clinically since the cantilever based system can be extended to any accessible epithelial or lumenal surface of the body, including the oral cavity and esophagus. Also, the actuation employed is electromagnetic actuation, which eliminates the need for electrical wires passing through the body.

2. Develop and characterize a wireless batteryless pressure sensing system for esophageal manometry applications.

   Current esophageal manometry systems are catheter based. These systems require physicians to do frequent invasive monitoring in case of moderate to severe esophageal cancer cases. Our approach provides a real time, on-demand manometry information without any invasive procedure. We have used planar interdigitated capacitor for pressure measurements. The planar design helps in measuring radial pressure as well as the changes in the axial directions. Additionally, they can provide flexibility of placement around commercial stents without affecting the stent performance.

1.3 Dissertation Organization

This work is organized as follows: Chapter 2 presents background information and cites the current literature on the optical coherence tomography based imaging systems. Chapter 3 provides an initial study on the design, and material properties of the imaging system components including cantilever and ferromagnetic materi-

als. Chapter 4 reports the dynamic characterization of the cantilever based system using different materials, and imaging feasibility of the miniature spectral optical coherence tomography system on human tissue. Chapter 5 presents the background information and cites the current literature on therapeutic systems for esophageal manometry applications. It also explains the design, materials and fabrication process for the capacitance based sensing platform. Chapter 6 discusses the integration of interdigitated capacitance sensor on a biocompatible polymer with a modulated batteryless wireless system using an *in vitro* system. Feasibility of using the interdigitated capacitor for measuring the axial strain is also discussed. The biocompatible polymer was then replaced with a biodegradable polymer and the performance of the system was analyzed. Chapter 7 summarizes and discusses the important findings and implications of this work.

CHAPTER 2

INTRODUCTION TO OPTICAL COHERENCE TOMOGRAPHY

2.1 Introduction

Optical coherence tomography (OCT) is an interferometric imaging technique with a wide range of applications in the field of biomedical imaging. OCT employs near-infrared light which is able to penetrate significantly deeper into the scattering medium [10]. Imaging of the internal microstructure in biological systems is done by measuring backscattered or backreflected light from the biological tissue. An OCT image is a two-dimensional or three-dimensional data set that represents differences in optical backscattering or backreflection in a cross-sectional plane or volume. Some of the main advantages of OCT are

- High depth resolution
- High transverse resolution
- Contact-free operation
- Non-invasive
- Instant, direct imaging of tissue morphology
- No preparation of the sample or subject
- No ionizing radiation

OCT synthesizes cross-sectional images from a series of laterally adjacent depth-scans from the light scattering media. This technique is being explored over a decade [11] to reveal the morphological structures of biological tissues and other samples. OCT employs a Michelson interferometer [12] with a low coherence broadband light source. Configuration of a Michelson interferometer is shown in Fig. 2.1. It consists of

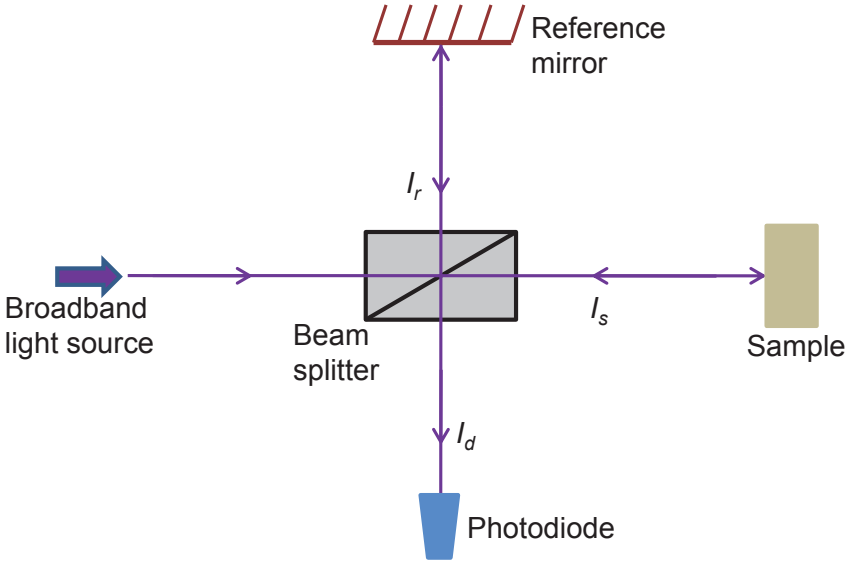

Figure 2.1. Schematic of a typical Michelson interferometer.

a broadband light source which is split into a reference path and a sample path. The reflected beams from the reference path (intensity=I_r) and the sample path (intensity=I_s) are recombined (intensity=I_d) at the beam splitter. This recombined beam with intensity I_d contains the interference information. A property of low coherence interferometry is that interference which is a series of dark and bright fringes is obtained only when the path difference lies within the coherence length of the light source. If the sample path and the reference path both have the same reflectivity, the interference is called auto correlation. When the reflectivities are different, it is called cross-correlation. In order to image a target, the path lengths of the reference path and sample path should be equal. OCT systems can be broadly classified into two types based on the principle used to estimate the depth information as:

1. Time domain optical coherence tomography (TD-OCT)
2. Spectral domain optical coherence tomography (Spectral OCT)

In a TD-OCT system, the reference mirror in the interferometer setup is rapidly scanned to match the optical path from reflections within the sample. This provides a depth profile (A-Scan) within the sample which is detected by a point photodiode. An OCT image is then constructed by stacking several A-scans that are laterally displaced in a direction orthogonal to A-scan (B-Scan) [13–15]. In TD-OCT, the photodetector detects the averaged intensity I_d, of the interference signal between the light reflected back from the reference path and the sample path. If there is a path delay of τ between the sample and the reference paths and if $\Gamma(\tau)$ is the coherence function between the two waves, then I_d is given by [16],

$$I_d = I_s + I_r + 4\sqrt{I_r I_s}\,\mathrm{Re}\left[\Gamma(\tau)\right]$$

One of the main drawbacks of TD-OCT is that the scan depth is decided by the scanning system on the reference arm. This can be easily overcome using a spectral OCT system in which there are no moving parts on the reference side. The reference path length is fixed and the detection system is replaced with a spectrometer.

In spectral OCT the depth information is obtained by measuring the spectral density at the detection arm of the interferometer with the help of a spectrometer [17]. The depth profile or A-scan is then obtained by taking the inverse Fourier transform of the spectral density. The use of a fast spectrometer has made video-rate imaging with this technique possible [18–21]. OCT has also been used in gastroenterology for early diagnosis of tumors [22], and images delineating substructures of mucosa and submucosa in GI organs have been reported [23].

2.2 General Spectral OCT System Design

In our configuration (Fig. 2.2), a broadband superluminiscent diode (SLD) light source (Broadlighter D830) guides the light into a fiber optic coupler which splits the light into two optical paths, a reference path and a sample path. The reference path is collimated and terminated with a mirror, while the sample path contains a scanning system that focuses the light onto the sample. Backscattered or reflected light from the sample path, and the reflected light from the reference arm path is recombined and directed into a spectrometer. The spectrometer spatially separates the light to form the interference pattern which is then analyzed to yield spectral OCT image. At any given scanning position, the sample arm path collects both the backscattered and the reflected light originating from different depths within the sample. Due to various depths within the sample, a modulation in the amplitude of the sinusoidally varying interference pattern occurs. Since the amplitude modulation is depth dependent, the Fourier transform yields the intensity of the backscattered or reflected light as a function of the depth[1].

The spectral density S(ω) obtained from the spectrometer consists of three terms [16]:

- Spectrum of light from the reference path
- Spectrum of light from the sample path
- Interference information representing the scan depth

Spectral density $S(\omega)$ is related to coherence function $\Gamma(\omega)$ by,

$$S(\omega) = \int_{-\infty}^{\infty} \Gamma(\omega) e^{(i\omega\tau)} d\tau$$

[1]Note: The colors in Fig. 2.2 are illustrations to show that the light travels to certain depth inside the sample

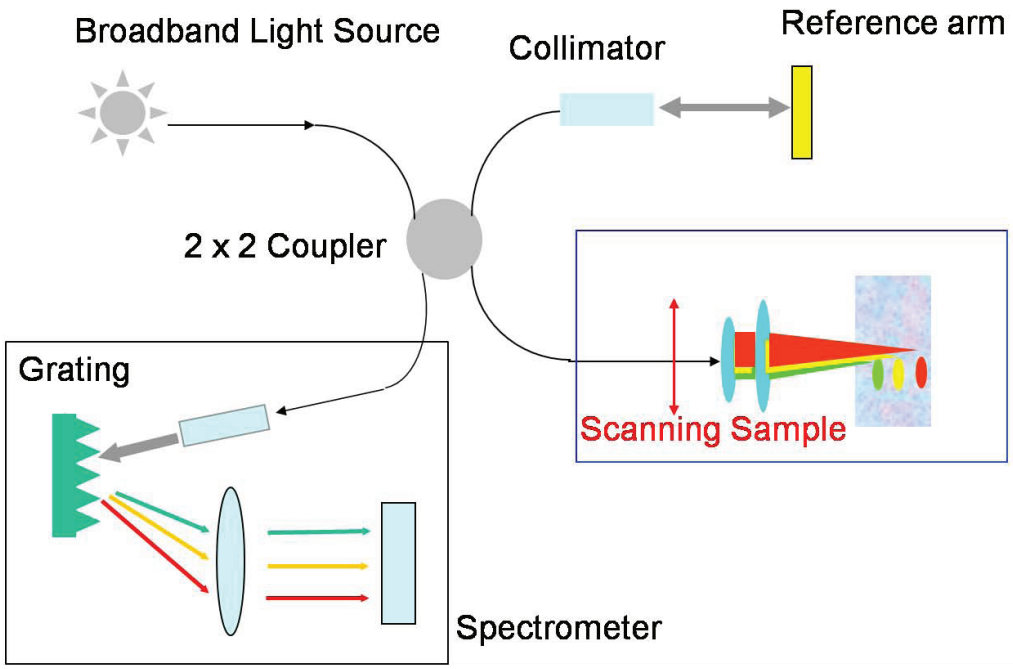

Figure 2.2. Schematic showing the principle of spectral OCT system.

For interference,

$$\Gamma(\tau) = |k_r|^2\Gamma(\tau) + |k_s|^2\Gamma(\tau) + k_r^* k_s \Gamma(\tau + t_1 - t_2) + k_r k_s^* \Gamma(\tau + t_2 - t_1)$$

where,

- t_1 and t_2 are the time taken by the light to traverse the reference arm and sample arm respectively
- k_r and k_s are the complex constants that represent the reflectivity of the objects in the reference and the sample arm
- $S_r(\omega) = |k_r|^2 S(\omega)$ and $S_s(\omega) = |k_s|^2 S(\omega)$ are the spectral densities of reference and the sample arm respectively
- G(ω) is the cross-spectral density between $S_r(\omega)$ and $S_s(\omega)$ having the depth information

$$S(\omega) = S_r(\omega) + S_s(\omega) + 2\,\mathrm{Re}\left[G(\omega)e^{\{i\omega(t_1-t_2)\}}\right]$$

The spectrometer can be used to detect the spectral density $S_r(\omega)$ by blocking the reflected light intensity from the sample path. The spectral density $S_s(\omega)$ is obtained by replacing the sample with a mirror and blocking the reflected light intensity from the reference arm. Thus, we can get the depth resolved information of the sample at a given spot using the interference spectrum. The spectrometer measures intensity as a function of the wavelength λ. Reconstruction of the axial scan depth $a_s(z)$ (which is function of depth z) is accomplished by evenly spacing the spectrum in wavenumber k ($k = 2\pi/\lambda$ is the Fourier conjugate of z). The amplitude of the reflected light is considered as unity. Then, the interference signal *I(k)* is given by [12],

$$I(k) = S(k)\left[1 + \frac{1}{2}F\left[a_s(z)\right] + \frac{1}{8}F\left\{R[a_s(z)]\right\}\right]$$

where $R[a_s(z)]$ is the autocorrelation due to the interference. Inverse Fourier transform of the above equation gives,

$$F^{-1}\left[I(k)\right] = F^{-1}\left[S(k)\right] \otimes \left[\delta(z) + \frac{1}{2}a_s(z) + \frac{1}{8}R[a_s(z)]\right]$$

Thus, the axial scan intensity a_s at any desired depth z can be obtained. The resolution of the spectral OCT system depends on the coherence length of the source. The coherence length of a Gaussian spectrum with a center wavelength, λ_o and full width half maximum, λ_{FWHM} is given by [24],

$$l_c = \left(\frac{4\ln(2)}{\pi}\right)\frac{\lambda_o^2}{\lambda_{FWHM}}$$

So far we have shown that the axial intensity and the depth information can be obtained from the interference spectrum of the spectral OCT system. In order to obtain a 2D or 3D image, a fast scanning system is needed in the sample path.

2.3 Scanning Systems

MEMS devices and fiber optical devices have several advantages in the field of endoscopy. They can provide small dimension profiles, fast speed, and high precision. The compactness of the optical devices makes them suitable for applications in which size, precision and low power consumption is critical. Fiber optical devices have been extensively used in the fields of telecommunications (such as fiber optical switches, and optical amplitude modulator) [25–27], medical imaging [28], and sensors [29–32]. Fiber optical devices have been developed with piezoelectric [25], electrostatic [26,33], thermal [34,35], and electromagnetic [11,36,37] actuation. Table 2.1 shows the typical device dimensions, power requirements and performance by using these actuation mechanisms.

Table 2.1. MEMS based actuators

System	Size/material	Power requirement	Output
Electrostatic [33]	2.25mm × 2.25mm × 3μm thick polyimide with gold coated mirror	25 to 50V	112 to 146^o at 41Hz
Electro-thermal [35]	150μ long × 1μ wide polysilicon	5280mW (210mA)	250μm displacement
Piezoelectric [28]	8μm × 200μm × 1000μm	300V	7μm displacement
Magnetic [36]	1.1mm × 1.1mm × 0.7mm thick SOI wafer with magnetic film	2V	8^o at 800Hz

Piezoelectric materials belong to a a category of materials which can produce an electric charge when subjected to mechanical stress. Conversely under an electric field, the piezoelectric material can deform due to mechanical stress. Some of the common piezoelectric materials are Lead zirconate titanate (PZT), Gallium orthophosphate, Barium titanate and polyvinylidene fluoride (PVDF). Boppart et. al. (1997) reported a PZT scanner that was 6.4mm $\times$ 72.1mm for for OCT imaging. Even though the scanning distance was 2mm (with 12μm axial and 31μm transverse resolutions), it required a very high input voltage of 300V for actuation. Gilchrist et. al. (2009) [38] reported a PZT based mirror which could achieve a tilt of $\pm 7^o$ and used a high input voltage of 40 volts.

Thermal actuators work on the principle of thermal expansion amplification in which a small amount of thermal expansion of one part of the device translates to a large deflection of the overall device. When electric current passes through a path with two different resistivities, the path with higher resistivity (hot arm) heats up more and pushes the other path that has lower resistivity (cold arm) provided the arms are constrained. Cochran et. al. (2005) reported thermal actuator based optical switch with a maximum displacement of 250μm at an input current of 160mA. The temperature of this actuator was more than 800^oK. Hence these devices have inherent limitations for long term use due to high temperature and high power consumption.

Electro-static actuators are based on coulomb attractive and repulsive forces. When two unlike charged bodies are brought closer together they experience attractive forces. These electrostatic forces will generate displacements. Zara et. al. (2003) reported an electrostatic scanning mirror employing an input voltage of $\pm$65 volts with a scanning distance of more than 3mm. Even though these actuators can achieve higher displacements, they require very high input voltage.

Optical devices using electromagnetic actuation, on the other hand, provide higher force, and larger deflection with lower power consumption. Nagaoka (1999) reported an electromagnetic actuation based fiber scanner in which an iron-nickel magnetic alloy pipe was fixed on an optic fiber for use as a scanner. The scanning distance was 150μm (at frequency of 500Hz) when the switch was actuated using an electromagnet (15mA and 0.6V). Even though the deflection was less, the power consumption is very low. Also, the force generated due to the magnetic field was very high (500μN) which can be compensated for lower scanning frequency.

Currently there are a few commercial OCT systems. Figure 2.3a shows a hand-held OCT system by Thorlabs. The dimension of the imaging head 115mm (long) $\times$ 50mm (wide) $\times$ 50mm (high) makes it very bulky and hence not suitable for our *in vivo* application.

(a) (b)

Figure 2.3. Commercial OCT systems (a) Thorlabs Inc., and (b) Galvo mirror by Cambridge Technology.

Other commercial OCT systems are based on galvo mirrors (as shown in Fig. 2.3b). A galvo system consists of a galvanometer (dimension 15.88mm diameter by 51mm long) mounted with mirror (7.8mm $\times$ 5.5mm). These Galvanometers employs motors that rotate the mirror and can reach scanning frequencies of more than 12kHz. However these scanner are very bulky and not suitable for *in vivo* applications. Taking into consideration the size, precision, force, speed and power consumption, devices with electromagnetic actuation provide better performance. Therefore we have used electromagnetic actuation based system for optical coherence tomography. The complete system design, fabrication and characterization is presented in following chapters (3 and 4).

CHAPTER 3

MINIATURE SPECTRAL OCT SYSTEM

Scanning system for a spectral OCT system can be implemented in a number of ways. In particular, the electromagnetic actuation has the advantage of producing larger force with low power consumption [36]. For example, permalloy of 1mm × 1mm × 5μm in size can generate a lifting force of about 87μN under a magnetic field of 2×10^4 A/m [39]. In our proposed design, the scanning system is replaced by a miniature plastic cantilever coated with ferromagnetic gel actuated using external electromagnetic field.

3.1 Magnetic Actuation Principle

A schematic of the cantilever based magnetic actuator is shown in Fig. 3.1. It consists of a cantilever structure fabricated using plastic which is then coated with a ferromagnetic gel. Actuation is achieved by using external electromagnetic field. Due to the electromagnetic field of the external electromagnet, the cantilever oscillates in a manner suitable for scanning. We have used a rectangular PVC plastic as the cantilever and nickel mixed with enamel paint as the magnetic gel. An optical assembly (consisting of optic fiber, glass ferrule and gradient refractive index lens) which is connected to the sample arm of a spectral OCT system can be mounted on the cantilever to obtain images with depth information. Some of the properties affecting the scanning are dimensions of the cantilever, magnetic material and position of the coating material. We have used mechanical and magnetic analysis to study the

scanning behavior of the electromagnetically actuated cantilever based spectral OCT system.

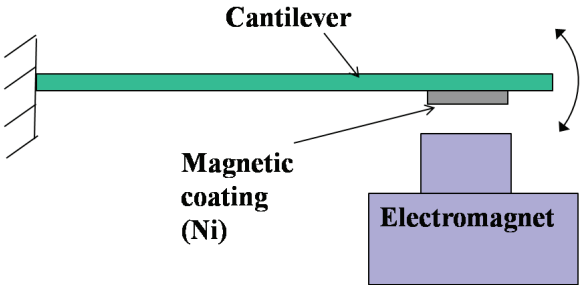

Figure 3.1. Magnetic scanner principle.

3.2 Mechanical Analysis

When a cantilever is subjected to a force F, the longitudinal axis of the cantilever deviates from its original position due to bending as shown in Fig. 3.2. The bending moment at any section is given by [40],

$$M = EI\frac{dv^2}{dx^2} \tag{3.1}$$

where E = Young's modulus of the cantilever, I = moment of inertia, and v = displacement of the cantilever along the Y-axis. For a rectangular cantilever of length L, width W and thickness t, the area moment of inertia is given by,

$$I = \frac{Wt^3}{12} \tag{3.2}$$

Figure 3.2 shows the cantilever with ferromagnetic gel being taken into consideration

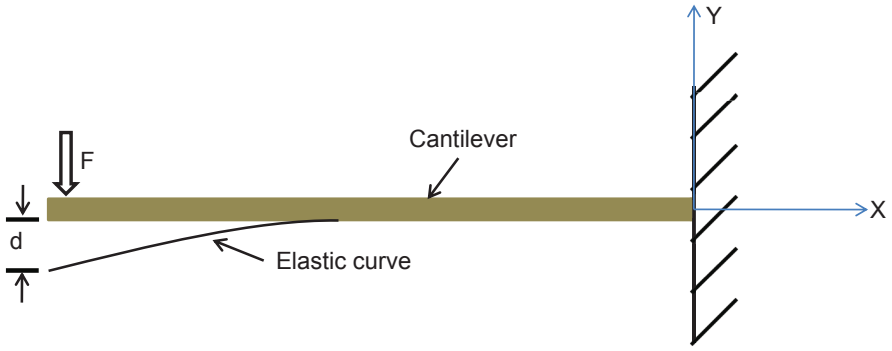

Figure 3.2. Cantilever bending due to an applied force.

for the behavior of cantilever bending. The bending moment due to the spring force F_{spring} at a distance x is given by

$$M = -F_{spring} \times x \tag{3.3}$$

Comparing Eqs. (3.1) and (3.3), we get

$$\int \left(EI \frac{dv^2}{dx^2} \right) = \int (-F_{spring} \times x) \tag{3.4}$$

$$\int EI \frac{dv^2}{dx^2} = \int -F_{spring} \times x$$

$$EI \frac{dv}{dx} = -\frac{F_{spring} \times x^2}{2} + C_1$$

At x=l, the bending slope is zero. So,

$$C_1 = \frac{F_{spring} \times l^2}{2}$$

$$EI \frac{dv}{dx} = -\frac{F_{spring} \times x^2}{2} + \frac{F_{spring} \times l^2}{2} \tag{3.5}$$

$$\int \left(EI\frac{dv}{dx} \right) = \int \left(-\frac{F_{spring} \times x^2}{2} + \frac{F_{spring} \times l^2}{2} \right)$$

$$EIv = -\frac{F_{spring} \times x^3}{6} + \frac{F_{spring} \times l^2 x}{2} + C_2$$

At x=l, the displacement in the the Y-direction is zero. So,

$$C_2 = -\frac{F_{spring} \times l^3}{3}$$

$$EIv = -\frac{F_{spring} \times x^3}{6} + \frac{F_{spring} \times l^2 x}{2} - \frac{F_{spring} \times l^3}{3} \tag{3.6}$$

Using Eq. 3.5, the bending slope of the cantilever at x=0 is given by

$$Slope = \frac{dv}{dx} = \frac{F_{spring} \times l^2}{2EI} \tag{3.7}$$

Similarly from Eq. 3.4, the deflection of the cantilever at x=0 is

$$v = -\frac{F_{spring} \times l^3}{3}$$

Since the negative sign only indicates that the displacement of the cantilever is downward, the magnitude can be written as

$$v = \frac{F_{spring} \times l^3}{3} \tag{3.8}$$

Expressing in terms of the spring force F_{spring}, the above equation becomes,

$$F_{spring} = \frac{3EI}{l^3} v = K^{'} v$$

where $K^{'}$ is the linear spring constant. In a magnetically actuated system, this force, F_{spring} is the spring restoring force that counteracts the magnetic force generated due to the electromagnetic field. For our miniature spectral OCT system, the loading is as shown in Fig. 3.3 in which the total deflection of the cantilever, d is the sum of the following components,

1. Deflection of the cantilever at point B due to the magnetic force and
2. Deflection due to slope of the cantilever which is equal to slope of the cantilever from point B to A multiplied by the distance between the point B and the tip A.

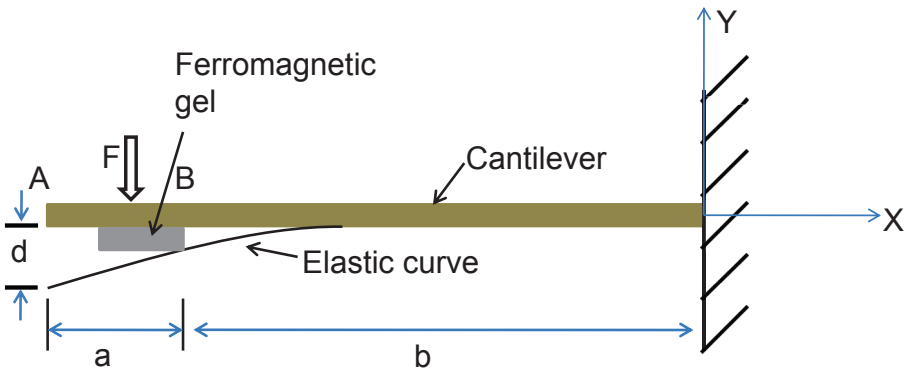

Figure 3.3. Loading of the cantilever due to self weight and magnetic coating.

Using Eqs. (3.7) and (3.8), the total linear deflection is given by

$$d = \frac{F_{spring}b^3}{3EI} + \frac{F_{spring}a^3}{2EI}$$

The spring restoring force and the spring constant can be obtained by rearranging the above equation.

$$F_{spring} = \frac{d}{\left(\frac{b^3}{3EI} + \frac{a^3}{2EI}\right)} = Kd \tag{3.9}$$

Thus for a given cantilever with magnetic coating, the spring restoring force is directly proportional to the scanning distance since all the other parameters are constant.

3.3 Magnetic Analysis

Ferromagnetic materials contain microscopic regions called domains within which all magnetic moments are aligned. The boundaries between various domains having same orientations are called domain walls. In a non-magnetized sample, the domains are randomly oriented so that the net moment is zero. When the sample is placed in an external magnetic field, the magnetic moments of the domain start to align with the magnetic field resulting in a magnetized sample. If the magnetic field is applied for a long time, the sample becomes saturated. Saturation of the sample depends upon the material, and volume of the sample. These processes are illustrated in Fig. 3.4. When the nickel based ferromagnetic gel is exposed to magnetic field, the domains start aligning with the magnetic field, which results in the bending of the cantilever as shown in Fig. 3.4(b). When all the domains are aligned the sample saturates and maximum displacement is achieved as illustrated in Fig. 3.4(c).

For a soft magnetic material like nickel, the total magnetic magnetic force is given by [41, 42] ,

$$F_{magnetic} = (m \cdot \nabla) H_0$$

where

- H_0 is the applied magnetic field
- m is the dipole moment equal to $\mu_0 MV$
- M is the magnetization vector
- μ_0 is the permeability
- V is the volume of the ferromagnetic gel

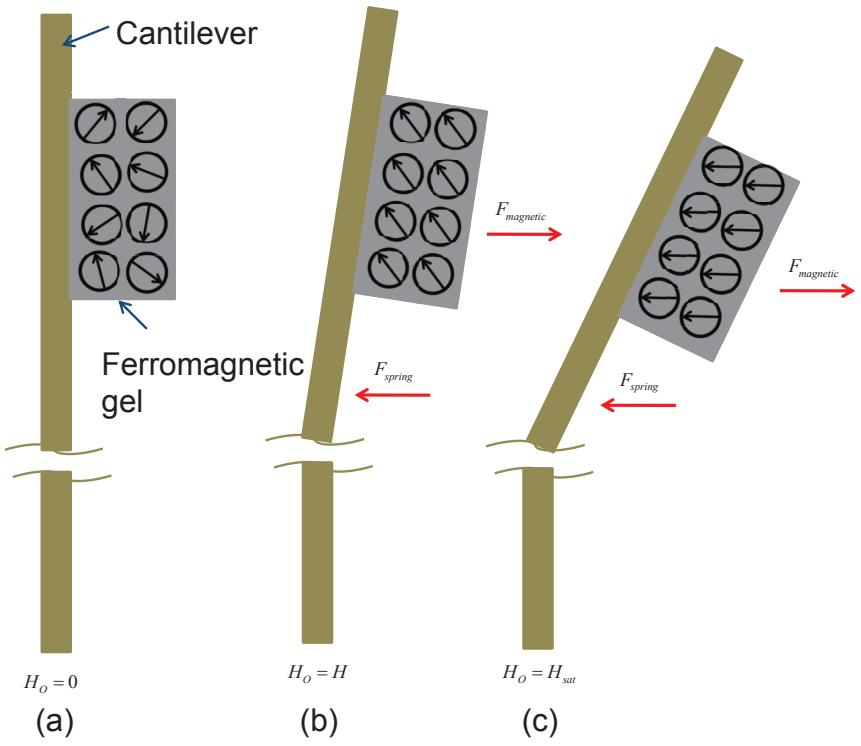

Figure 3.4. Magnetic field for (a) non-magnetized (b) magnetized and (c) saturated ferromagnetic gel sample.

$$F_{magnetic} = \mu_0 MV\,(\nabla H_0)$$

$$F_{magnetic} = \mu_0 MV\left(\frac{dH_0}{dx} + \frac{dH_0}{dy} + \frac{dH_0}{dz}\right)$$

In our configuration, magnetic field is highest in the Z-direction and the magnetic fields in X- and Y-directions can be neglected. Hence,

$$F_{magnetic} = \mu_0 MV\frac{dH_0}{dz} \tag{3.10}$$

Thus the magnetic force is directly proportional to the gradient of the magnetic field since permeability, magnetization and volume are constant for a given ferromagnetic gel.

3.4 Displacement and Resonant frequency

Our design employs a cantilever coated with ferromagnetic gel actuated by an external electromagnetic field. In order to accurately determine the position of the cantilever, the magnetic force and the spring restoring force should be in equilibrium. That is,

$$F_{spring} = F_{magnetic}$$

From Eqs. 3.9 and 3.10,

$$\frac{d}{\left(\frac{b^3}{3EI} + \frac{a^3}{2EI}\right)} = \mu_0 MV \frac{dH_0}{dz}$$

$$d = \mu_0 \cdot M \cdot V \cdot \frac{dH_0}{dz}\left(\frac{b^3}{3\,E\,I} + \frac{a^3}{2\,E\,I}\right) \tag{3.11}$$

Thus for a given system, the displacement of the cantilever is directly proportional to the applied electromagnetic field. To get the maximum deflection, the cantilever should oscillate at its resonant frequency [43]. Additionally, the cantilever consumes less power at resonance. Using Rayleigh's method [43], for a cantilever with optical fiber of mass m_c carrying a concentrated mass m_g of ferromagnetic material the mechanical resonant frequency is given by [2],

$$f = \frac{1}{2\,\pi}\sqrt{\frac{3\,E\,I}{l^3\,(m_c + 0.23\,m_g)}} \tag{3.12}$$

From these analyses, the force, the displacement and the resonance characteristics of the cantilever based actuation system were obtained. This can be used to optimize the system performance either by changing the cantilever dimension or the magnetic material.

3.5 Ferromagnetic Materials and Their Properties

In this section, we have characterized different ferromagnetic materials and their saturation volume densities, coercivity fields, and remnant fluxes to identify the materials best suited for our application.

The miniature spectral OCT scanner has been characterized to ensure that its behavior is accurately predicted by the theory and the physical principle. Magnetic materials are classified by their magnetic coercivity or hardness. Materials with low coercivity are called soft materials and those with high coercivity are called hard materials. Low coercivity materials are suitable for low power and high speed applications because the magnetic remnant flux can be removed with low reverse magnetic field [40]. In our design, with low-cost fabrication in mind, we chose three different non-magnetized ferromagnetic materials to characterize and compare their performance. As opposed to magnetized ferromagnetic materials, which give rise to magnetic torques under the influence of external magnetic field, non-magnetized ferromagnetic materials such as nickel, cobalt and iron are attracted to external magnetic fields. This phenomenon can be utiltized to obtain the dynamic displacements of the miniature spectral OCT scanner.

The magnetic properties of the ferromagnetic materials were characterized using a MicroMag alternating gradient magnetometer (AGM) [44]. Measurements were carried out with a layer of ferromagnetic gel sample placed parallel to the external magnetic fields in order to minimize the demagnetization effect. A sample of ferromagnetic gel was mounted on an extension rod attached to a piezoelectric element of the AGM. This rod was then placed at the center of the poles that generated magnetic fields. An alternating gradient magnetic field produced an alternating force on the poles which in turn acted on the sample. This force was converted into a proportional voltage by the piezoelectric element and the moment of the sample was measured.

Various magnetic materials were experimentally analyzed in their non-magnetized forms since the ferromagnetic gel was not magnetized. The particle size and densities of these materials are shown in Table 3.1. For example, 99.99% pure nickel powder with an average particle size of 3.5μm and a density of 8.91g/cm^3 was used in the experiment. The ferromagnetic gel was prepared by combining nickel powder and enamel paint in the ratio 30:70 by weight. The magnetic gel was mixed using a delicate brush and coated on a thin planar paper film. The 0.1mm thick film was allowed to dry in air for about 20 minutes and a sample of 3mm $\times$ 2mm area was cut and transferred to the AGM. Figure 3.5 shows the measured coercivity field H_c, remnant flux M_r, and saturation flux M_s.

Table 3.1. Physical properties of ferromagnetic materials [1, 2]

Material (99.99% purity)	Particle Size (μm)	Density (g/cm^3)
Nickel (Ni)	3.5	8.91
Cobalt (Co)	0.5 to 1.5	9.92
Iron (Fe)	44	7.87

Similarly, results for iron and cobalt are shown in Figs. 3.6 and 3.7. The coercivity fields of cobalt, nickel, and iron are 10.76kA/m, 6.78kA/m, and 2.13kA/m respectively in their non-magnetized bulk form. Saturation volume densities are tabulated in Table 3.2 and they are well above the actuation magnetic field intensity (15.9kA/m) of the electromagnet. Therefore the nickel, cobalt and iron coatings can be used for actuation without exceeding their saturation limits.

Thus, our proposed miniature spectral OCT system uses a cantilever based scanner with a ferromagnetic gel coating to achieve scanning. The analysis of the cantilever suggests that the displacement of the cantilever is directly proportional to

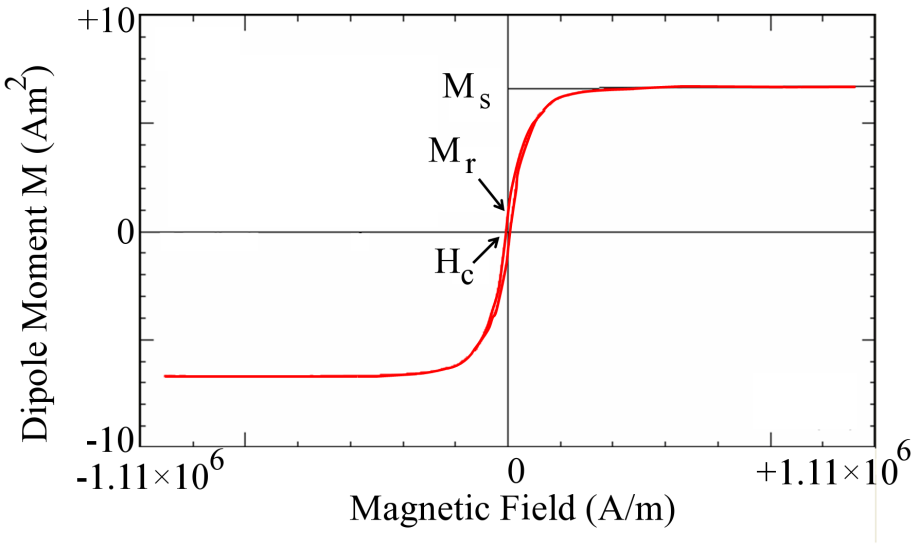

Figure 3.5. Magnetic hysteresis curves for non-magnetized nickel.

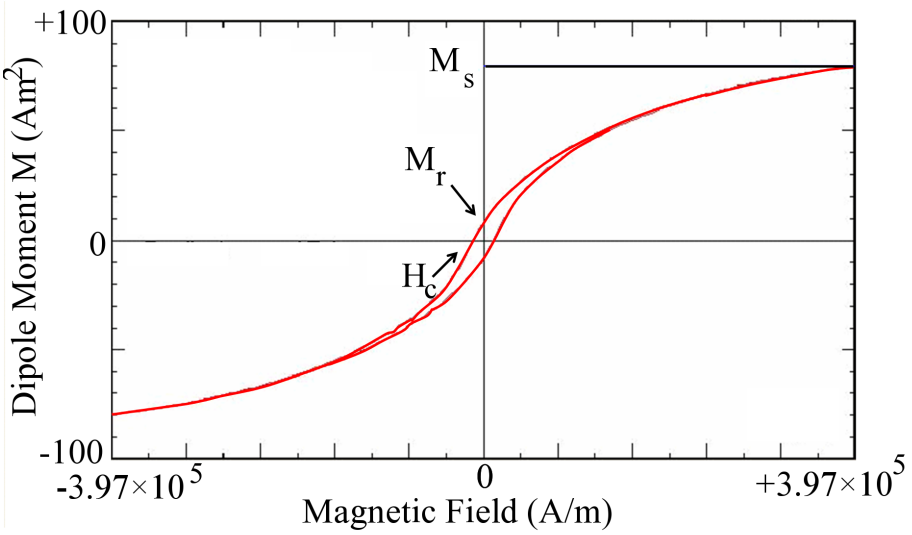

Figure 3.6. Magnetic hysteresis curves for non-magnetized cobalt.

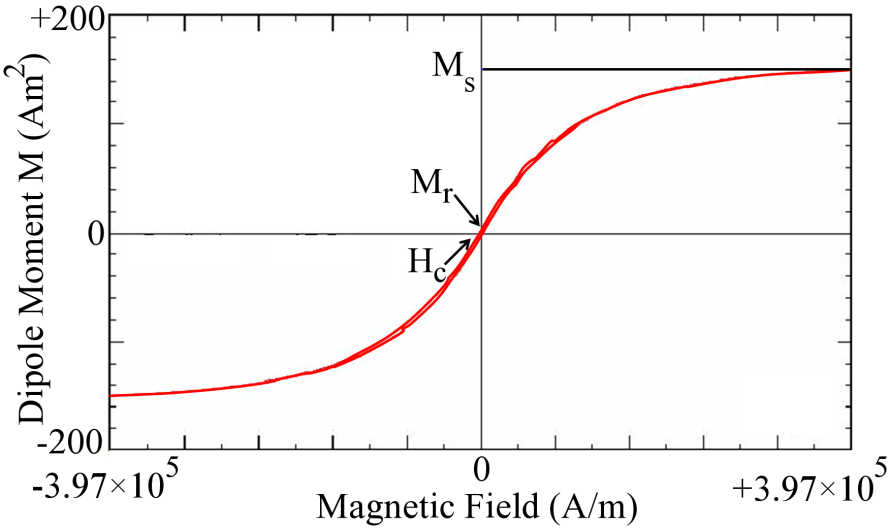

Figure 3.7. Magnetic hysteresis curves for non-magnetized iron.

Table 3.2. Magnetic properties of ferromagnetic materials

Material	Coercivity H_c (A/m)	Remnant flux M_r (Am^2)	Saturation flux M_S (Am^2)	Saturation volume density (kA/m)
Nickel (Ni)	6783.9	0.975	6.67	37.07
Cobalt (Co)	10766.83	8.228	79.64	353.95
Iron (Fe)	2139.83	3.1	149.8	832.22

the applied magnetic field. The system performance of a cantilever based scanner can be changed by changing the dimensions of the cantilever and by using different ferromagnetic coatings. The experiments with ferromagnetic materials indicate that actuation distance of the cobalt coated cantilever will be higher compared to the nickel and iron coated cantilever systems. The design, fabrication and analysis of a miniature spectral OCT system is discussed in detail in chapter 4.

CHAPTER 4

OCT EXPERIMENTS

4.1 Introduction

Spectral OCT provides faster speeds with better imaging quality and simplicity in a system setup. The challenges were to design, fabricate and characterize a scanning system that can be easily integrated with the OCT system. The scanning required the capability for miniaturization and adaptability for the desired application environment. Towards this goal, we proposed a ferromagnetic gel coated cantilever based scanning system, actuated by an external electro-magnetic field. This technique does not require any electrical wires connected to the scanning cantilever. The advantages of the proposed system is that magnetic actuation is suitable for constructing *in vivo* steerable probes that can provide a larger force (tens of micro Newtons) that can compensate for the device speed and scanning range. To achieve translating forces a nickel based coating was used for its high permeability (which provides higher magnetic field) and low coercivity (which provides low field strength and faster scanning speeds).

4.2 Fabrication

In our design, we propose to use a cantilever coated with ferromagnetic gel for scanning. In order to make the gel, the ferromagnetic material was mixed with enamel paint. The mixture was prepared by combining the ferromagnetic material with enamel paint in the ratio of 1:1 by weight. This mixture was then molded into a cuboid: 7mm (long) $\times$ 2mm (wide) $\times$ 0.5mm (thick). The gel was allowed to harden at

room temperature for about 20 minutes and attached to the cantilever at a distance of 5mm from the free end using an adhesive epoxy. The image of the cantilever coated with ferromagnetic nickel gel coating is shown in Fig. 4.1. The dimension of the rectangular cantilever beam is 70mm (long) × 2mm (wide) × 0.77mm (thick). For a rectangular cantilever, the oscillations are restricted along one plane increasing the linearity and stabilty of the scanner. Hence, we chose a rectangular configuration [43]. Our fabrication technique employs simple, and repeatable fabrication processes suitable for mass production and does not include expensive equipment or time-consuming processes.

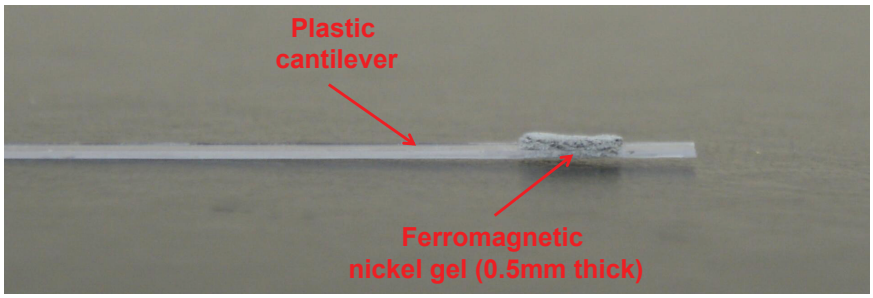

Figure 4.1. Image showing a 70mm long plastic cantelever with 0.5mm thick ferromagnetic nickel gel coating.

4.3 Finite Element Analysis

Finite element analysis using ANSYS [45] was performed to optimize the dimensions of the cantilever and to obtain the resonant frequency of the cantilever. The material properties of the cantilever used in the analysis are summarized in Table. 4.1. Mechanical boundary condition is applied by defining $u_x = u_y = u_z$=0. For simplicity,the effectof damping on the cantilever due to air is not considered. Mesh sensitivity analysis was also performed in order to ensure that the solution obatined

was mesh independent. It was found that for a cantilever 70mm long by 2mm wide and 0.77mm thick, the resonant frequency is 28Hz as shown in Fig. 4.2. Additionally, for a cantilever of 60mm long with same width and thickness as before, the resonant frequency was 38.1Hz (Fig. 4.3). The 60mm design was used to verify if the design parameters were valid when used with ANSYS. These simulation results were experimentally verified.

Table 4.1. Cantilever Material Properties

Parameter	Value
Young's modulus	1359.4MPa
Poisson's ratio	0.42
Density	1.14g/cm^3

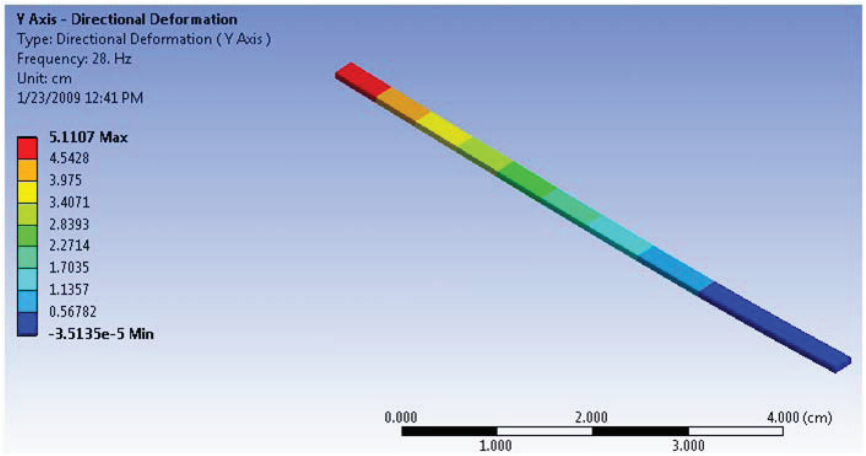

Figure 4.2. Analysis of 70mm long cantilver design.

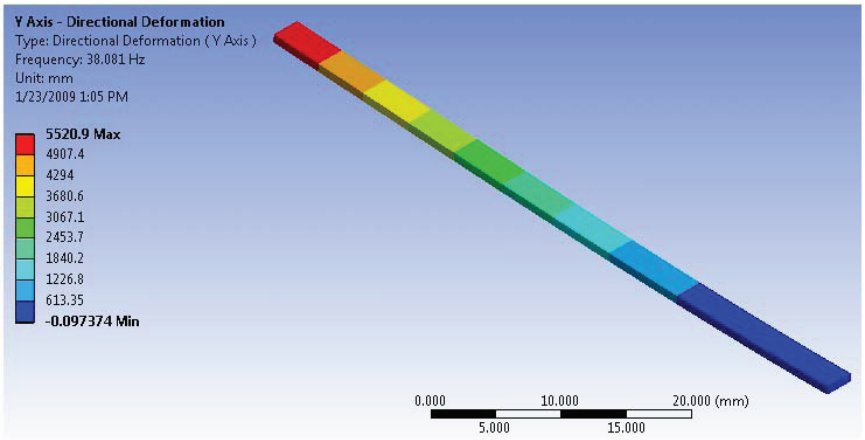

Figure 4.3. Analysis of 60mm long cantilever design.

4.4 Experimental Setup for Dynamic Analysis

The experiment setup for the dynamic measurement is shown in Fig. 4.4. To perform dynamic analysis, an AC voltage is applied to the electromagnet. The cantilever (with the ferromagnetic gel and the optic fiber) was held tightly using a clamping fixture. The fiber optic cable was fixed on the cantilever in a way not to allow it to affect the motion of the cantilever. A 2.5-mW diode laser (632.8 nm) was coupled to the optic fiber throught a FC/APC connector. The electromagnet has a frequency bandwidth of 60Hz and a resistance of 30Ω. The magnetic field strengths of the electromagnet at different distances from its magnetic core were measured experimentally using an F. W. BELL 5080 Gaussmeter. A position sensitive detector (PSD) (as shown in Fig. 4.5) was placed 1mm from the output of the fiber to detect the position of the incident laser spot. The output currents of PSD were converted to voltages by connecting a 100kΩ resistor in series with each electrode of the PSD (One Dimensional PSD S3932, Hamamatsu Corporation). The oscilloscope monitored the output voltage waveforms of the PSD when AC voltage was applied to the electromagnet. The laser beam spot on the PSD active area was 0.3mm in

diameter giving a current output in the milliampere range and the voltage output in the millivolts range. The photo sensitivity of PSD at 632.8-nm wavelength is 0.4A/W. The driving frequency applied to the electromagnet was increased gradually until the amplitude of the PSD waveform reached a maximum indicating the fundamental resonance. Figure 4.6 shows the output waveform from the the two PSD electrodes. It can be seen that the scanning frequency of the cantilever based magnetic scanner is twice that of the driving frequency.

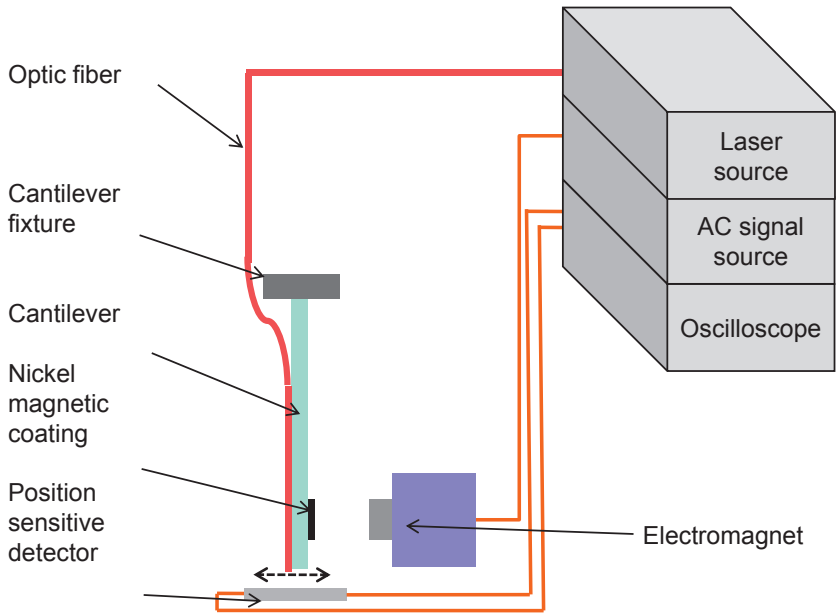

Figure 4.4. Experimental setup for dynamic characterization.

The doubling of the scanning frequency can be explained as follows. When the ferromagnetic gel is magnetized within the first half of the positive cycle of the driving current, the poles are opposite and the cantilever scanner is attracted towards the electromagnet. It reaches maximum displacement, when the magnetic force is equal to the spring force. During the second half of the positive cycle the magnetic fields start to decrease and the spring force pulls the cantilever back. The momentum of the

cantilever moves the scanner to the other endpoint. Again, the spring force pulls the fiber back during which the pole on the electromagnet facing the gel is reversed by the current in the first half of the negative sinusoid. The ferromagnetic material starts magnetization and the poles become opposite again so the cantilever is now attracted by the electromagnet until it reaches the maximum displacement. During the second half of the negative cycle, the cantilever moves away by the spring force and repeats the motion similar to the one in the positive cycle of the driving current. Hence, for every driving cycle in the electromagnet, the cantilever completes two cycles of scanning resulting in doubling of the frequency.

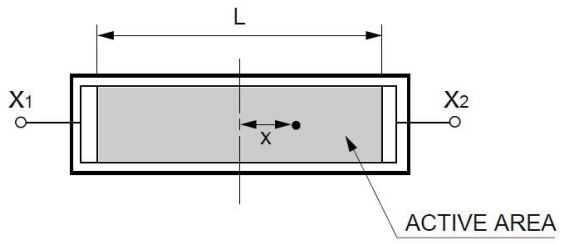

Figure 4.5. Schematic of a position sensitive detector with an active area length L showing a laser spot at a distance x from the center.

Experiments were carried out with two different lengths of cantilever, 60mm and 70mm to verify the design parameters used in finite element analysis. Figure 4.7 shows the frequency spectrum for the 70mm long cantilever system. We can see that at the resonant frequency of 29Hz a maximum scanning distance of 1.4mm can be achieved. Additionally, when the scanner is made to oscillate at lower and higher frequencies (other than resonant frequency), the scanning distance reduces rapidly. Table 4.2 shows comparison of the resonant frequency obtained from the finite element analysis with that of the experimental results for the two cantilever lengths, 60mm and 70mm. It can be seen that the simulation and experimental results match closely. In

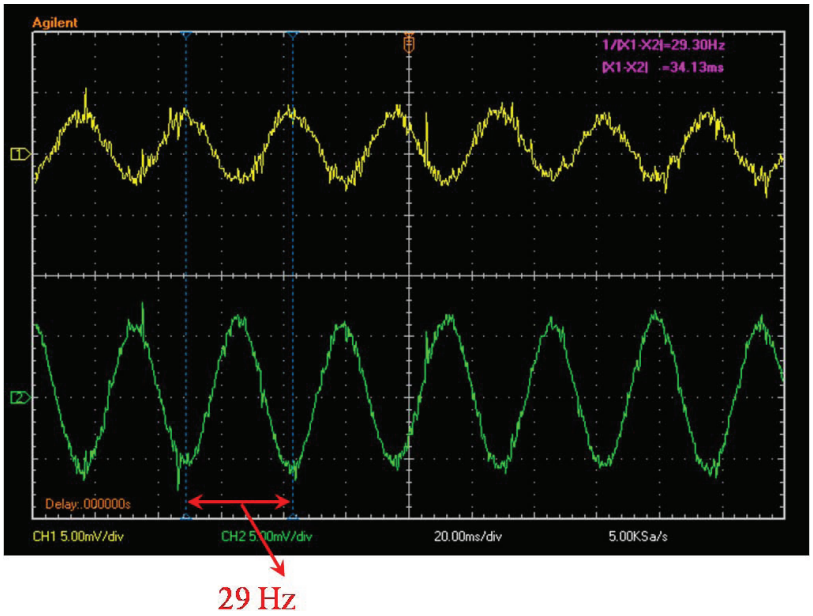

Figure 4.6. Typical output wavefroms from two electrodes of the position sensitive detector.

order to demonstrate feasibility of imaging on human tissue, an integrated miniature spectral OCT employing cantilever based scanning system was built and tested using the 70mm long cantilever design.

Table 4.2. Comparison of experiment and simulation results

Cantilever Length (mm)	Resonant Frequency from FEA (Hz)	Resonant frequency from experiment (Hz)
70	28	29
60	38.1	36

4.5 Integrated Spectral OCT system

The ferromagnetic gel was prepared by mixing 50% nickel and 50% enamel paint by weight. A 0.5mm thick ferromagnetic gel coating was attached on a plastic

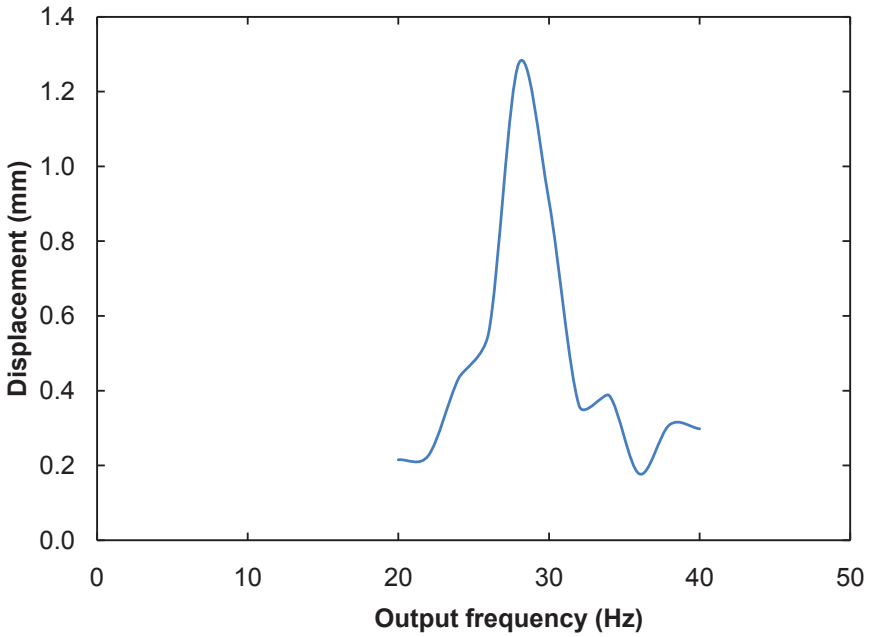

Figure 4.7. Dynamic displacement of the 70mm long cantilever system.

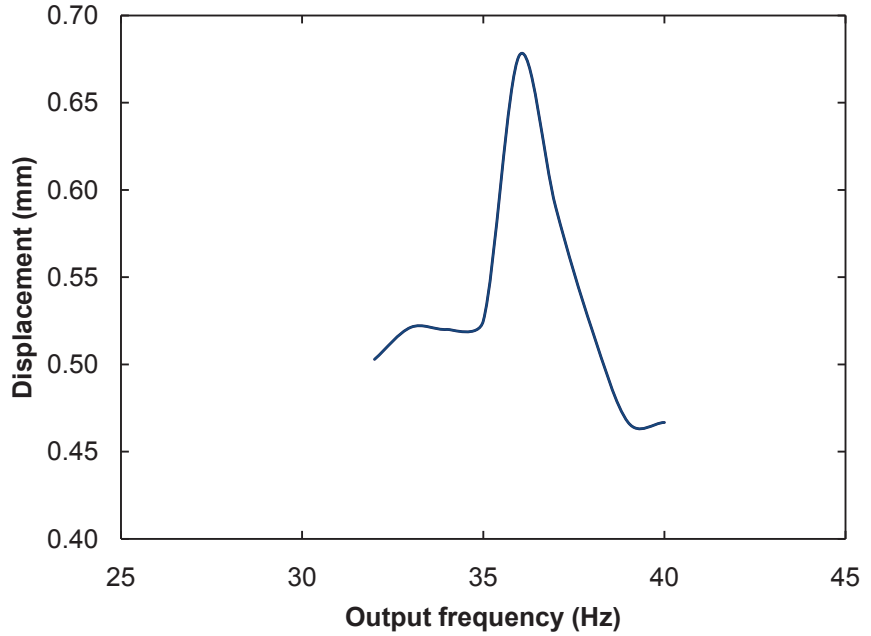

Figure 4.8. Dynamic displacement of the 60mm long cantilever system.

cantilever 5mm away from the tip of the cantilever using epoxy. An optical assembly mounted on the cantilever can then be steered using an external magnetic field source. The overall device dimension is 3.19mm (thick), 0.64mm (wide) and 70mm (long) . For the given dimensions the experimental resonant frequency was determined to be 28Hz. Figure 4.9 shows schematic of the spectral OCT system with the optical assembly on one side of the cantilever and the ferromagnetic coating on the other side. The fixed end of the cantilever was attached to a clamping mechanism. A glass optical fiber ferrule with an outer diameter of 1mm is used to mount and fix the position of an 8^o cleaved optic fiber. The optical fiber is angle cleaved to eliminate the back reflection due to the refractive index mismatch of the media. A gradient refractive index (GRIN) lens was mounted 0.4mm away from the cleaved fiber end and focal point was 3.8mm from the lens. The optical assembly was firmly attached using an epoxy. The pigtail optical fiber having FC/APC connector can be connected as the reference path of the spectral OCT system.

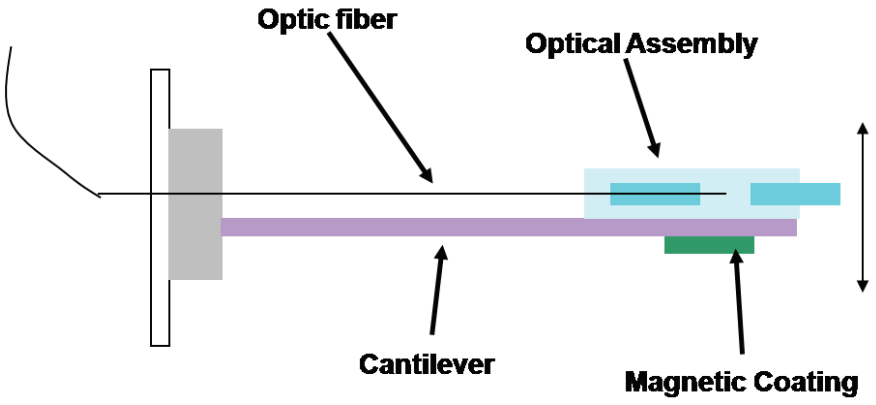

Figure 4.9. Schematic of the miniature spectral OCT system employing magnetic actuation.

The optical modulation efficiency of the system was 87% and the maximum power onto the sample was 2mW. The magnetic probe is used to perform *in vivo*

imaging on human finger nail. Figure 4.10 shows the cross-sectional image of finger extending from the cuticle portion to the finger nail clearly showing the layered structure underneath. The images were taken at 40 frames per second with an input AC triggering voltage of 14V to the electromagnet. The maximum scanning range of 1.4mm and a scanning depth of 600μm was achieved.

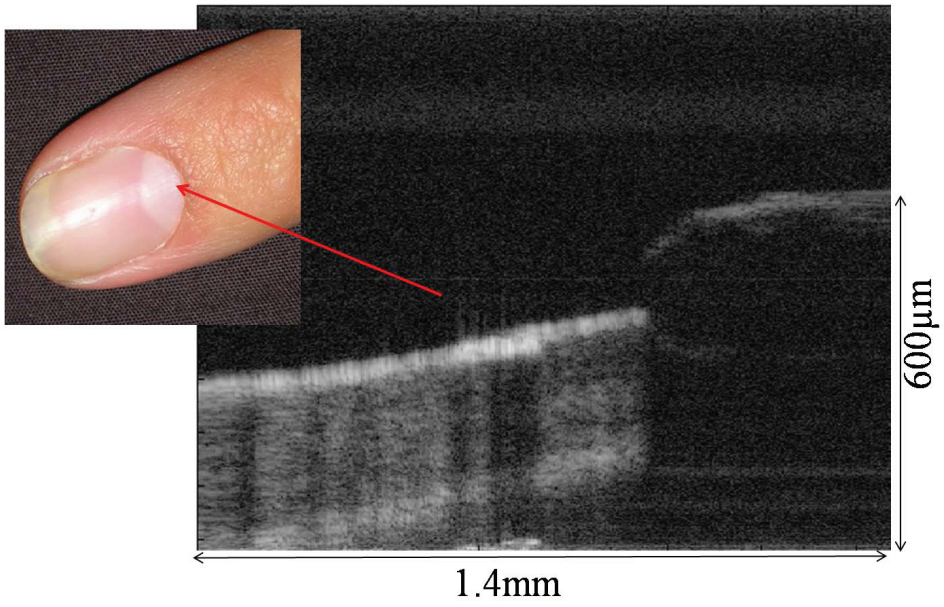

Figure 4.10. Image showing cuticle of the index finger using the miniature spectral OCT system.

4.6 Design Optimization

The scanning range of the imaging system discussed in the previous section can be modified by changing the ferromagnetic magnetic material and/or length of the cantilever. Three ferromagnetic materials nickel, cobalt, and iron powder were separately tested. Actuation cantilever lengths of 60mm, 70mm, and 80mm, with

the same rectangular cuboid of ferromagnetic gel were fabricated to investigate the maximum deflection and the mechanical performance.

4.6.1 Fabrication

The ferromagnetic material was mixed with an enamel paint in the ratio 50% enamel paint and 50% ferromagnetic nickel powder by weight. This mixture is then molded into a cuboid: 7mm(long) by 2mm (wide) by 1mm (thick). It was found that the thicker ferromagnetic gel helped in achieving higher scanning range. The gel was allowed to cure and harden at room temperature for 20 minutes and attached to the cantilever (of dimension 70mm(long) by 2mm (wide) by 0.77mm (thick)) at a distance of 5mm from the free end using adhesive. Cobalt and iron cuboid samples were fabricated to the same dimensions as nickel. Figure 4.11 shows the three cantilever scanners coated with ferromagnetic iron, nickel and cobalt coatings.

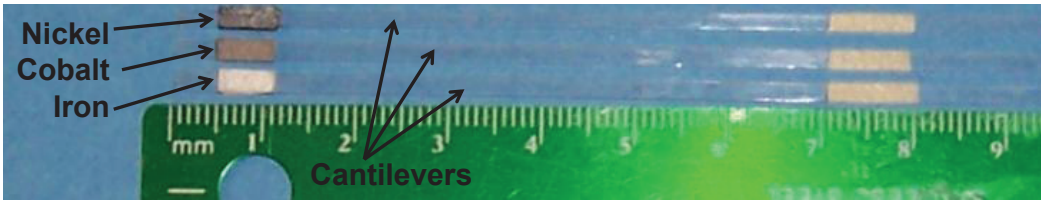

Figure 4.11. Image shows plastic cantilevers coated with 1mm thick ferromagnetic nickel, cobalt and iron gels.

4.6.2 Results

A dynamic analysis was performed as discussed previously in section 4.4. It consists of an AC voltage source which feeds the electromagnet. The cantilever (with the ferromagnetic gel and the optic fiber) is held tight using a clamping fixture. The fiber optic cable is fixed on the cantilever in a way not to allow it to affect the motion

of the cantilever. A 2.5-mW diode laser (632.8 nm) was coupled to the optic fiber using a FC/APC connector. A position sensitive detector (PSD) was placed 1mm from the output of the fiber to detect the position of the incident laser spot. The output currents of PSD were converted to voltages by connecting a 100kΩ resistor in series with each electrode of the PSD (One Dimensional PSD S3932, Hamamatsu Corporation). The oscilloscope monitored the output voltage waveforms of the PSD when AC voltage was applied to the electromagnet. The input driving frequency to the electromagnet was increased gradually until the amplitude of the PSD waveform reached maximum indicating the fundamental resonance. Figure 4.12 shows the results for cantilever scanner coated with ferromagnetic iron. It can be seen that maximum scanning of 2.51mm can be obtained with the cantilever length of 80mm at the resonance frequency of 10.8Hz. As the length of the cantilever decreases to 70mm and 60mm, the resonance frequency increases to 13.8Hz and 16.8Hz respectively. The scanning distance also reduces to 2.07mm and 0.79mm respectively in the case of 70mm and 60mm long cantilevers.

Figures 4.13 and 4.14 show the scanning distance variation for nickel and cobalt coated cantilever for the three different lengths 60mm, 70mm and 80mm. For the ferromagnetic nickel coated cantilever, the maximum scanning distance was 3.27mm at the resonant frequency of 10.6Hz with 80mm long design while it was 4.97mm at the resonant frequency of 10.2Hz for the cantilever design with the same length. Table 4.3 summarizes the maximum scanning distances and their resonant frequencies of the cantilever scanner with the three different ferromagnetic materials iron, nickel and cobalt.

It can be seen that for a given cantilever length, cobalt has the highest scanning distance while iron had the highest resonant frequency. Additionally, for a given

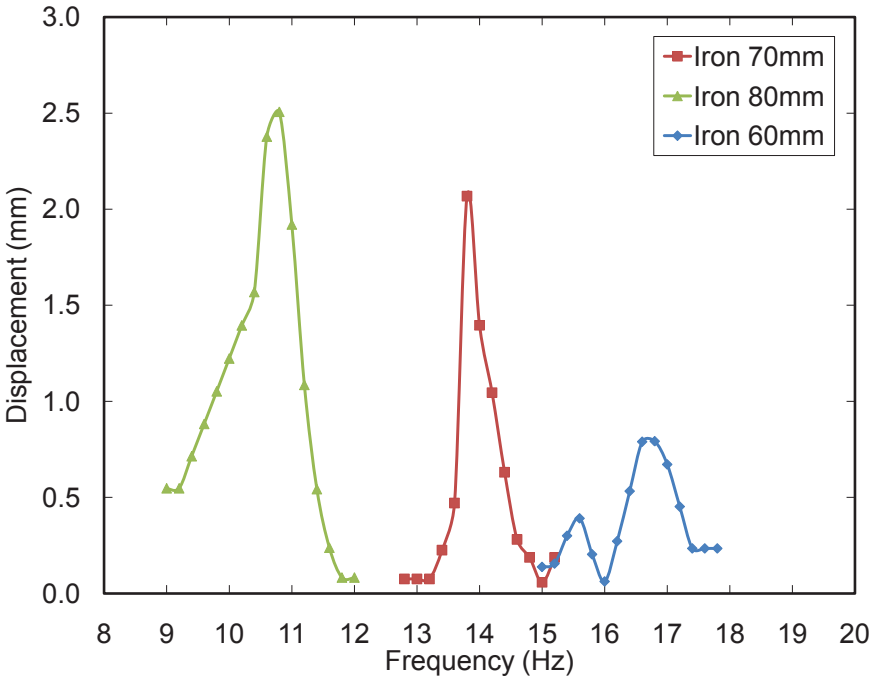

Figure 4.12. Dynamic analysis showing the ferromagnetic iron gel based cantilever system.

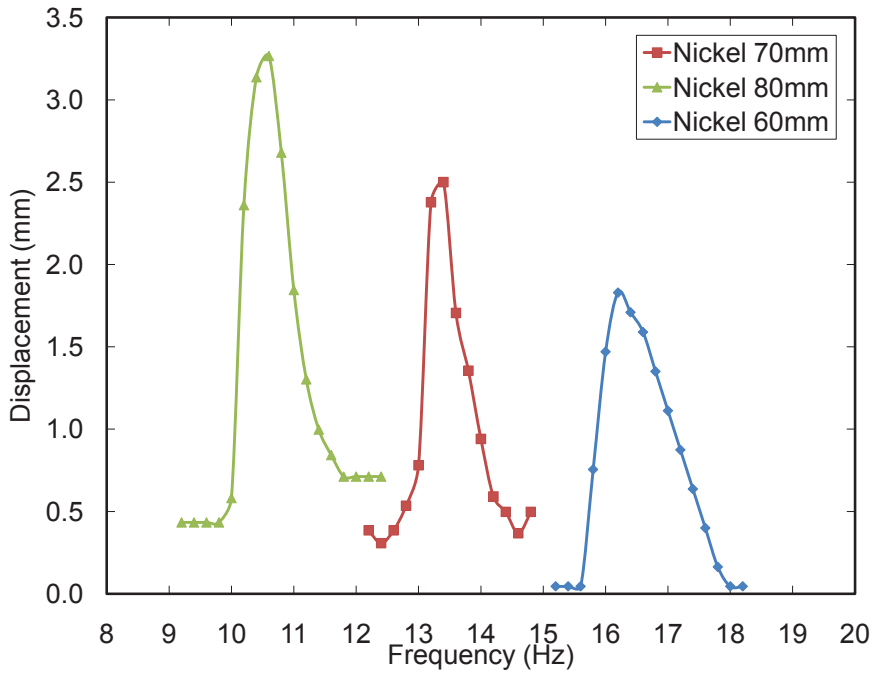

Figure 4.13. Dynamic analysis showing the ferromagnetic nickel gel based cantilever system.

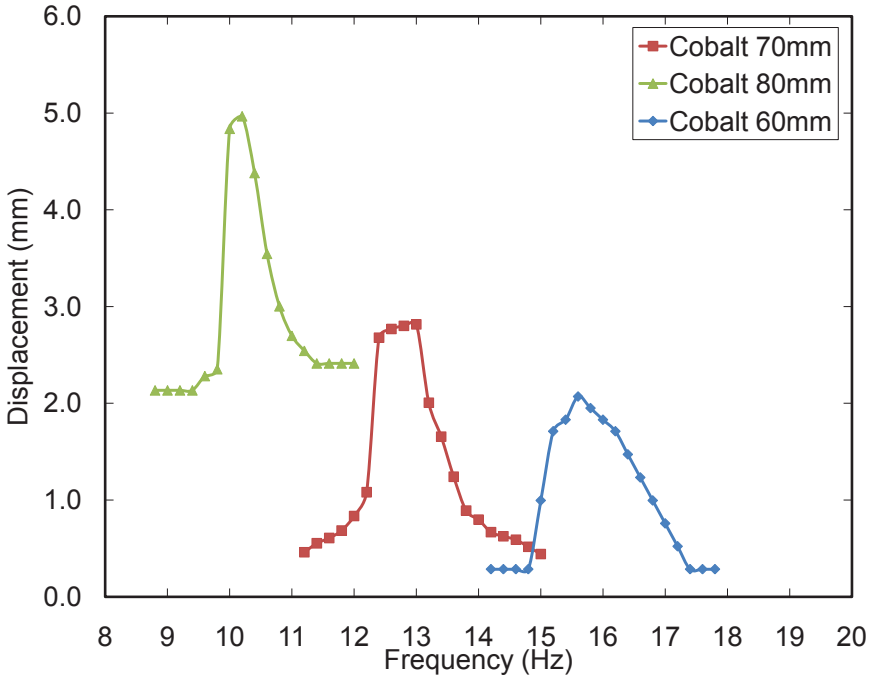

Figure 4.14. Dynamic analysis showing the ferromagnetic cobalt gel based cantilever system.

material, 80mm design had the highest scanning distance while 60mm design had the highest scanning frequency.

4.7 Summary

In this chapter, a magnetically-actuated *in vivo* miniature spectral OCT imaging probe employing spectral OCT has been demonstrated. An optical assembly is mounted on a ferromagnetic gel coated cantilever and steered with an external electromagnet. The finite element analysis results used for designing the cantilever scanner and the experimental results based on this design matched closely. For the 70mm long cantilever with a 0.5mm thick ferromagnetic nickel coating, the simulation and experimental resonant frequencies were 28Hz and 29Hz respectively. The simulation and the experimental resonant frequencies for 60mm long cantilever with 0.5mm thick

Table 4.3. Comparison of optimization results

Material	Cantilever length (mm)	Scanning distance (mm)	Resonant frequency (Hz)
Iron	60	0.79	16.80
	70	2.07	13.80
	80	2.51	10.80
Nickel	60	1.83	16.20
	70	2.50	13.40
	80	3.27	10.60
Cobalt	60	2.32	15.60
	70	2.82	13.00
	80	4.97	10.20

nickel coating was 38Hz and 36Hz respectively. An optical modulation efficiency of 87% for optical coherent tomography using a superluminiscent diode laser at 780nm with power of 2mW and a FWHM bandwidth of 49 nm was achieved at an imaging rate of 40 frames per second and a scanning range of 1.4mm using a ferromagnetic nickel based cantilever system.

The optimization of the scanning distance and the resonant frequency was performed using different ferromagnetic materials, nickel, cobalt and iron and for different cantilever lengths, 60mm, 70mm and 80mm. Cobalt showed the highest scanning length while iron showed the lowest scanning length for a given cantilever length. An 80mm long cantilever design had the highest scanning distance while a 60mm design had the highest resonating frequency for a given ferromagnetic material. The scanning distance with a 1mm thick gel was higher than that of the cantilever with 0.5mm thick coating. At the same time, the resonant frequency decreased with a thicker gel since the gel added some additional weight to the cantilever system. Thus, for devices with thicker coating, the scanning distance can compensate for the device

scanning speed. Thus, a cantilever with desired length and ferromagnetic coating can be chosen based on the specific scanning application requirement.

CHAPTER 5

ESOPHAGEAL CANCER AND MANOMETRY SYSTEMS

5.1 Motivation

Malignant cancer is characterized by uncontrolled growth and spread of abnormal cells which can lead to death. There are several causes of cancer such as inherited mutations, hormones, immune conditions and mutations that occur from metabolism. The risk is further increased by tobacco use, exposure to radiation etc. Cancer is treated with surgery, chemotherapy, hormone therapy, biological therapy and targeted therapy. In the United States, cancer is only second compared to heart disease [46] in terms of fatalities. Esophageal cancer is one of the deadliest cancers and is estimated to lead to 14,530 (11,490 male and 3,040 female) deaths in 2009 [47].

The esophagus is a muscular tube that extends from the neck to the abdomen and connects the mouth to the stomach. The lining of the esophagus is the most common region for cancers of the esophagus. Most of the length of the esophagus is lined with squamous cells. If these cells degenerate into a malignant tumor, it gives rise to a type of cancer called squamous cell cancer. The very bottom portion of the esophagus and the region where the esophagus and the stomach join are lined with columnar cells that can give rise to malignant tumors called adenocarcinoma. Other rare forms of esophageal cancer include sarcoma and small cell cancer.

Even with recent advances in diagnosis and treatment, more than 50% of esophageal cancers are inoperable [48, 49]. Palliative care is the principle goal of therapy for such patients. One of the significant effect of esophageal cancer is gradual blockage of the esophagus leading to inability to swallow. In these cases, esophageal

stenting is an effective form of treatment of malignant esophageal obstruction, providing a rapid, safe and effective symptomatic relief in most patients [50–52].

5.2 Stents

A stent is an expandable mesh or wire tube which is inserted into the esophagus using an endoscope under x-ray guidance. An esophageal stent is used to keep a blocked area open so the patient can swallow soft food and liquids (Fig. 5.1). Esophageal stents are made of metal mesh, plastic, or silicone. Some of the most common commercial stents are shown in Fig. 5.2. These stents are very expensive and do not incorporate any theraupeutic abilities or any ability to monitor the cancer/tumor growth. In high to severe cases the patients with stents needs frequent invasive monitoring by the physician to assess the condition of the stent and the growth of the tumors. In our design, we propose to use a novel miniature, passive wireless pressure sensor on a flexible substrate which can be used for gastrointestinal (GI) manometry applications. The sensor can be incorporated in metal or biodegradable esophageal stents for both therapeutic and diagnostic purposes.

Figure 5.3 shows the schematic of our proposed wireless design. It consists of wireless pressure sensor integrated with an esophageal stent, capable of transmitting manometry information without need for invasive systems.

The challenge was to design, fabricate and characterize a batteryless wireless pressure sensing system that would allow on-demand monitoring of pressure from the esophagus. Some of the main features of this system are:

- Planar design
- Batteryless
- Low power consumption
- Compact

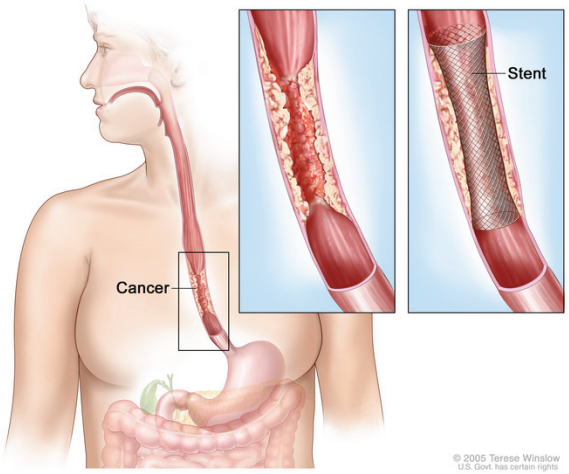

Figure 5.1. Schematic showing an esophageal stent used for palliative care (courtesy of National Cancer Institute).

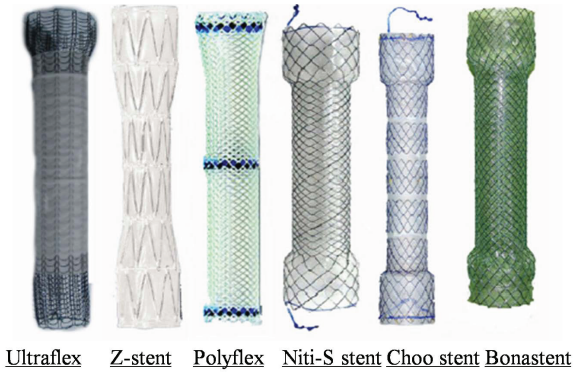

Figure 5.2. Image showing commercial esophageal stents.

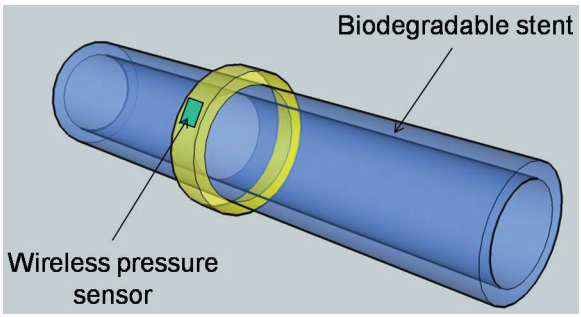

Figure 5.3. Schematic of a wireless passive pressure sensor integrated with a biodegradable stent.

- Low cost
- Employs biocompatible/biodegradable materials

The proposed design uses a capacitance based sensing system which is explained in the following section.

5.3 Capacitance Based Sensing System

Capacitive sensors draw no DC power and hence are favored for low-power and wireless applications [53]. They can be used in the form of passive inductor-capacitor resonant circuits for frequency based measurement of pressure [54–56]. Micromachined parallel plate capacitive pressure sensors typically use an elastic diaphragm with fixed edges and a sealed cavity in between the diaphragm and the substrate below [57,58]. These configurations rely on the deflection of a relatively thin diaphragm against a sealed cavity and has drawbacks of robustness of the diaphragm and leaks in the cavity seal. Larger displacements also require relatively large surface area of the parallel plates. There have been innovative fabrication methods that involve multilayer deposition, and planarization processes [59, 60] to improve the performance of sunch devices. However, these require higher mask counts which makes the fabrication expensive. In our wireless pressure sensing system design, we propose to use interdigitated capacitor (IDC) as the sensing element.

5.4 Interdigitated Capacitor (IDC)

IDC is a set of comb like periodic pattern of metal electrodes (fingers) deposited on a substrate making it in-plane unlike conventional parallel plate capacitors. The gap between the electrodes is filled with a dielectric material (the substrate or a secondary material that is deposited) to increase the capacitance when compared to

an airgap capacitor. By using a flexible substrate, the IDC can be made variable. In order to obtain the capacitance of an IDC, we start with a simpler parallel plate capacitor (Fig. 5.4) whose capacitance is given by

$$C = \frac{\varepsilon A}{x}$$

where

- ε is the dielectric constant of the medium between the plates
- x is the separation gap between the plates
- A is the surface area of the parallel plate

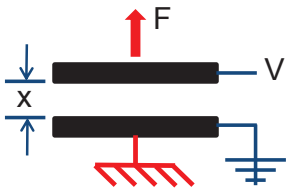

Figure 5.4. Schematic of a parallel plate capacitor.

When a force applied on one of the parallel plates increases the separation (as shown in Fig. 5.4), the capacitance decreases and vice versa. These capacitors are very bulky and the capacitance decreases rapidly as the force increases the separation between the plates. This can be overcome by using interdigitated capacitor (IDC) [61–63]. Figure 5.5 shows the schematic of an IDC with N fingers of length L and having an un-overlapped length x. The capacitance for a single finger is given by,

$$C_s = \frac{\varepsilon A}{2g}$$

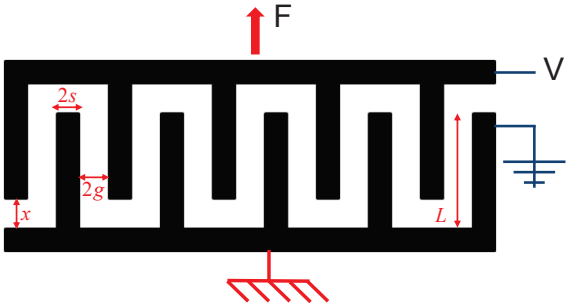

Figure 5.5. Schematic of planar interdigitated capacitor.

For an IDC of thickness t, this area is $A = t(L - x)$. So, the resulting equation for the capacitance is

$$C_{\mathrm{s}} = \frac{\varepsilon t(L - x)}{2g}$$

Since there are two capacitances for each finger, we get $2N$ capacitors. If we neglect the edge effects [64–66], the total capacitance is given by,

$$C = \frac{N\varepsilon t(L - x)}{g}$$

It can be seen that the capacitance is directly proportional to the overlapped length (L-x) and inversely proportional to the gap between the electrodes $2g$. This equation for capacitance is not accurate for a multilayer structure which has substrate and encapsulation dielectric effects. The capacitance is not only due to the dielectric material in between the electrode fingers but also from the top and bottom dielectric media as shown in Fig. 5.6. Capacitance C_1 is due to the electrode thickness t and the distance between the adjacent electrodes $2s$ is given by,

$$C1 = \frac{\varepsilon_o \varepsilon_2 t}{2s}$$

where ε_o is the dielectric constant of the free space (8.854×10^{-12}F/m), ε_2 is the dielectric constant of the encapsulation. C_2 and C_3 depends on the electrode width $2s$ and can be derived using conformal mapping technique by Gevorgian (1996) and can be written as [67–70],

$$C_2 = \varepsilon_o\varepsilon_e \frac{K\left(\sqrt{1-\left(\frac{s}{2(s+g)}\right)^2}\right)}{K\left(\frac{s}{s+g}\right)}$$

and

$$C_3 = \varepsilon_o\varepsilon_s \frac{K\left(\sqrt{1-\left(\frac{s}{2(s+g)}\right)^2}\right)}{K\left(\frac{s}{s+g}\right)}$$

where ε_s and ε_e are the dielectric constants of the substrate and encapsulation respectively, $K\left(\sqrt{1-\left(\frac{s}{2(s+g)}\right)^2}\right)$ and $K\left(\frac{s}{s+g}\right)$ are complete elliptical integrals of the first kind. The unit capacitance due to these three capacitances is given by,

$$C_u = C_1 + C_2 + C_3$$

$$C_u = \left\{\frac{2\varepsilon_o\varepsilon_2 t}{s}\right\} + \left\{\varepsilon_o\varepsilon_s \frac{K\left(\sqrt{1-\left(\frac{s}{2(s+g)}\right)^2}\right)}{K\left(\frac{s}{s+g}\right)}\right\} + \left\{\varepsilon_o\varepsilon_e \frac{K\left(\sqrt{1-\left(\frac{s}{2(s+g)}\right)^2}\right)}{K\left(\frac{s}{s+g}\right)}\right\}$$

If there are N fingers, then by symmetry, there are a total *N-1* unit capacitances per unit length. So, the total capacitance for an IDC with finger length L can be written as,

$$C = C_u(N-1)L$$

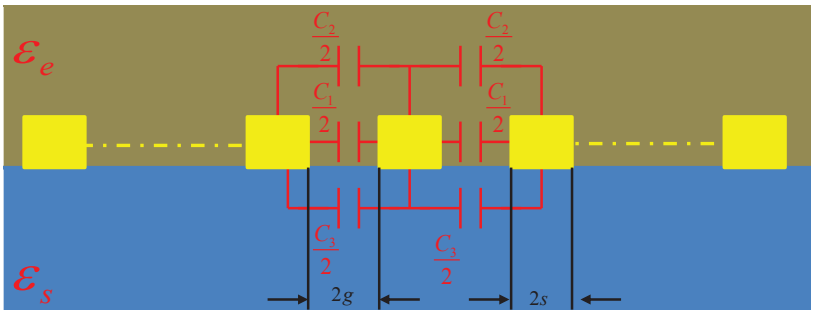

Figure 5.6. Schematic showing the crosssectional view of an IDC showing capacitances due to multilayer configuration.

In this equation for the total capacitance of interdigitated capacitor, the edge effects are neglected since the finger length is very large compared to the line width in our proposed design [71,72]. By calculating the capacitances at each of the interfaces and substituting in the above equation, we can calculate the approximate capacitance of the IDC. In later sections, we have compared the capacitance values obtained from experimental measurements of the fabricated IDC against the theoretical values. The following section discusses the fabrication process of the variable IDC in detail.

5.5 Fabrication of Variable IDC

To show the feasibility of using a variable IDC for pressure measurements we have used a polymer Polydimethylsiloxane (PDMS) as the substrate [73–75]. PDMS is commercially available and is also clean room compatible. The polymer is also biocompatible and could be used in applications requiring short term *in vivo* monitoring after which it can be removed. PDMS has the following advantages [76]:

1. Low elasticity change with temperature
2. High thermal stability
3. Good dielectric stability
4. Shear stability

5. High compressibility

Due to its high flexibility and very low drift in properties with time and temperature, PDMS is a good candidate for fabricating mechanical sensors such as our variable IDC.

PDMS is a two part polymer comprising of a base and a curing agent. Ten parts of the base was mixed with one part of curing agent to obtain a 10:1 PDMS polymer solution. This solution was spin coated on a glass wafer at 4000rpm for 30 seconds resulting in a 40μm thick PDMS layer on the glass wafer. The polymer coated wafer was cured on a hot plate at 60^oC for 60 minutes. To improve the adhesion properites of the cured polymer surface, a reactive ion etching (RIE) was performed in oxygen plasma. A layer of copper (0.4μm thick) was then evaporated on the RIE treated PDMS surface for the IDC structures.

A layer of Shipley S1813 positive photoresist was then spin coated on the metal layer. Photolithography process was used to transfer the required IDC patterns on the photoresist. The process steps are as shown in table 5.1. The wafer was then softbaked and developed in Microchem MF319 photoresist developer. The developing stage removes the photoresist in the region that needs etching of the copper surface. A post develop bake at 90^oC was used to harden the photoresist so it can withstand copper etching. The exposed copper regions were then etched using APS100 copper etchant at 40^oC for 30 seconds. A final RIE in oxygen plasma removes the photoresist that is covering the IDC patterns. Figure 5.7 shows several IDC structures fabricated on PDMS substrate using the above fabrication process.

PDMS being very flexible makes the electrical probing of devices for measurement of capacitance very difficult. Additionally, when the device was stretched, the capacitor metal patterns peeled off from the surface of PDMS. In order to keep the IDC structures intact, alternative substrates were considered. We chose 135μm thick

Table 5.1. Fabrication of IDC on PDMS substrate

Step	Process
1	Mix PDMS base and curing agent in the ratio 10:1
2	Degas PDMS in vacuum chamber to remove entrapped air in the solution
3	Spin coat PDMS on Pyrex substrate
4	Cure the polymer on hot plate
5	Evaporate thin-film
6	Spin coat, expose and develop photoresist using IDC mask to create IDC pattern on the evaporated metal
7	Soft bake photoresist
8	Solvent etching of thin film to create IDC metal patterns
9	Reactive ion etching to remove residual photoresist

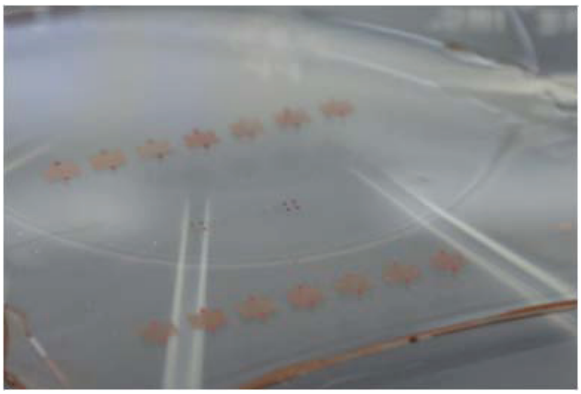

Figure 5.7. Fabricated IDC on PDMS substrate.

planar Kapton film due to its biocompatibility, thermal stability and excellent mechanical and chemical resistant properties. A new process was developed to fabricate IDC on Kapton. These IDCs can then be encapsulated by PDMS making the IDC variable. The fabrication steps are summarized in table 5.2. A clean 135μm thick Kapton sheet is laser machined using Oxford lasers E-355-3-OA system. This system uses a 355nm diode pumped laser with a maximum output power of 5W at 10kHz. The laser has a pulse width of 15ns. The laser system was fixed while beam delivery and focussing systems can be adjusted to get the desired spot size on the Kapton

substrate. A 2D stage which was programmed using CNC g-code was used to pattern the Kapton substrate with the desired IDC structure. The parameters, focus distance, speed and number of etch cycles were carefully characterized so as to reduce charring and retaining the properites of the Kapton substrate. The parameters are summarized in table 5.3.

Table 5.2. Fabrication of IDC on Kapton substrate

Step	Process
1	Laser machining of IDC structure on Kapton
2	Solvent clean and blow dry to remove laser etched debris
3	Evaporate thin-film
4	Mix PDMS base and curing agent in the ratio 10:1
5	Degas PDMS in vacuum chamber to remove entrapped air in the solution
6	Encapsulate IDC region with PDMS

Table 5.3. Parameters used for laser machining

Parameter	Value
Beam focus distance (mm)	83.15
Laser power (%)	5 to 10
Frequency (Hz)	500 to 750
Stage speed (mm/s)	0.5
Etch passes (#)	12 to 15

The parameters used were selected since they gave a constant IDC line gap and line widths of 35μm and 40μm respectively. A detailed machine code is given in appendix A. Figure 5.8 shows an IDC with 80 fingers (with L=1.5mm). Table 5.4 shows the IDCs fabricated with four different dimensions. The machined IDCs were

solvent cleaned and blown dry to remove any laser debris attached to the device. A thin metal film of 0.4μm thick copper was deposited using evaporation. Figure 5.9 shows an IDC with 60 fingers (with L=1.5mm) after copper deposition. The IDC structure is held intact by the two tethers on the left and right side of the IDC device. The IDC pattern was connected to retain its structure during the process steps by means of a tethering structure which holds the fingers together. De-tethering is done after the encapusation stage to get the final capacitor functionality by breaking the short circuited device after metal deposition.

Figure 5.8. Laser machined IDC structure on Kapton film.

A three step encapsulation by PDMS was used to make the IDC variable. A thin layer of 0.5mm thick PDMS mixture was cured in a Pyrex dish. The IDC was placed on the PDMS layer and the two electrode regions were protected. A second layer of 0.5mm thick PDMS solution is poured on the finger regions of the electrode. A partial cure was done on the PDMS and the tethers were broken using a fine blade. Some

Table 5.4. Dimensions of fabricated IDC

Device	Fingers	Finger length L (mm)	Line width (μm)	Space width g (μm)
1	60	1	40	35
2	60	1.5	40	35
3	80	1	40	35
4	80	1.5	40	35

more PDMS solution was added to fill up the gaps left behind by the de-tethering process and a final curing was done. PDMS was cured at room temperature in all the three stages. Figure 5.10 shows the image of the variable IDCs. Our fabrication process has several advantages. The planar structure of IDCs helps in mass production and also in conformal integration setup to achieve maximum sensitivity. Laser micromachining eliminated the photolithography and etching processes. Laser machining also helps in easy reconfiguration of IDC structure design without affecting the following fabrication processes. PDMS encapsulation makes the dielectric properties of the device stable keeping the external dielectric effects from the changing environment conditions to a minimum.

5.6 Characterization of Variable IDC

In order to demonstrate the feasibility of using the variable IDC for pressure sensing applications, the following characterization were performed on the 80 fingers (L=1.5mm) IDC:

1. Frequency dependence tests of the variable IDC
2. A linear tensile test to determine the capacitance vs. pull distribution
3. A finite element analysis to determine the force vs. pull for the variable IDC
4. Experimental verification of the force vs. pull analysis

Figure 5.9. Copper deposited IDC on Kapton film.

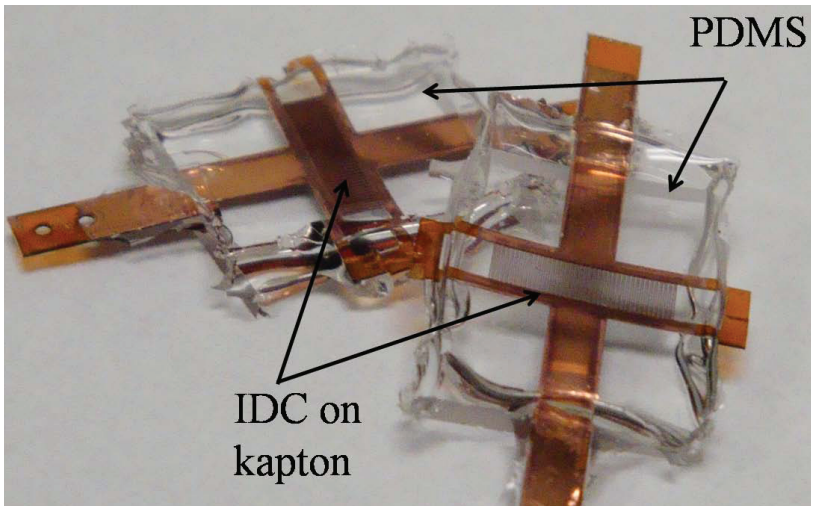

Figure 5.10. Image showing variable IDCs encapsulated in PDMS with 80 fingers (left) and 60 finger (right).

5.6.1 Frequency Dependance of Variable IDC

Planar capacitors have a frequency range over which the capacitance is stable. The capacitance of the fabricated IDCs were tested in a probe station (Micromanipulator model:8060-US8-V0-1-AA) using a precision LCR meter (Agilent Technologies model 4284A). The frequency of the LCR meter was varied between 20Hz and 1MHz. The variation of capacitance vs. frequency for the four IDC designs is shown in Fig. 5.11. It can be seen that the capacitances were stable in the range of 1kHz to 1MHz. As long as the variable IDC was used in the above frequency range, the instantaneous capacitance could be accurately determined. In our wireless pressure sensing system based on variable IDC, we have used an operating frequency between 10kHz and 20kHz.

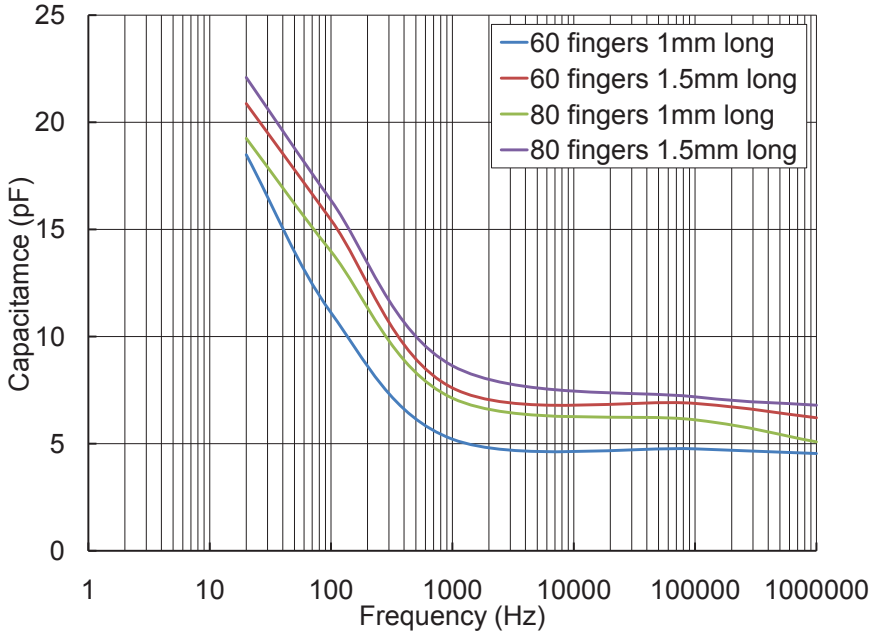

Figure 5.11. Experimental results showing frequency dependence of different variable IDCs.

Table 5.5 compares the capacitance values measured by an LCR meter and the ones obtained from theoretical analysis (section 5.4) at a frequency of 1kHz. The dielectric constants of the substrate and the encapsulation were obtained from the polymer data sheet. A difference of approximately ±11.56% was observed between the theoretical and experimental results. This could be due to the fact that experimental measurements may not be perfect and may include some external interference and parasitic capacitances. In our proposed wireless pressure sensing system, the variable IDC will be used to measure the change in capacitance and not the absolute value. Hence the difference between the theoretical and experimenal value of IDC has no significant effect on the functioning of the pressure sensing system. In order to analyze the capacitance behavior under a known pull, a linear tensile test was performed as discussed in the following section.

Table 5.5. Comparison of theoretical and experimental capacitance values of IDC employing PDMS encapsulation

Device	Substrate dielectric constant (ε_s)	Encapsulation dielectric constant (ε_e)	Unit capacitance	Total IDC capacitance from theory (pF)	IDC capacitance from experiment (pF)
80 fingers, 1.5mm	3.3	2.3	7.97E-11	9.45	8.63
80 fingers 1mm	3.3	2.3	7.97E-11	6.30	7.12
60 fingers, 1.5mm	3.3	2.3	7.97E-11	7.06	7.6
60 fingers, 1mm	3.3	2.3	7.97E-11	4.70	5.21

5.6.2 Linear Tensile Test

The experimental setup for the linear tensile test is shown in Fig. 5.12 in which one end of the IDC was fixed using a clamping fixture. The free end was clamped to a micrometer controlled stage which can stretch the varible IDC in one direction. AWG 34 magnetic wires were soldered to the two exposed electrodes of the variable IDC and connected to a Agilent 4192A impedance analyzer for measuring the instantaneous capacitance. The micrometer was rotated clockwise in steps pf 0.05mm to stretch the variable IDC and the resulting capacitance was measured. Figure 5.13 shows the resulting capacitance variation due to linear pull. It can be clearly seen that, as the pull increases from 0 to 1mm, the capacitance of the variable IDC decreases from 8.4pF to 5.4pF. These results were consistent even with repeated experimental cycles, showing that variable IDC can be used in our wireless pressure sensing system.

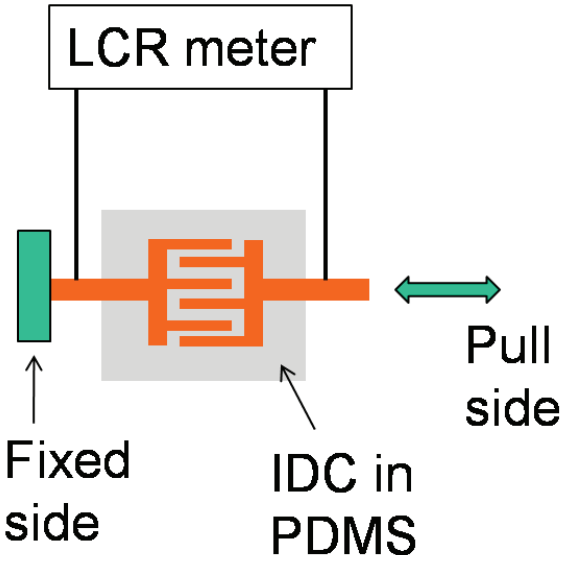

Figure 5.12. Schematic showing experimental setup for linear tensile test.

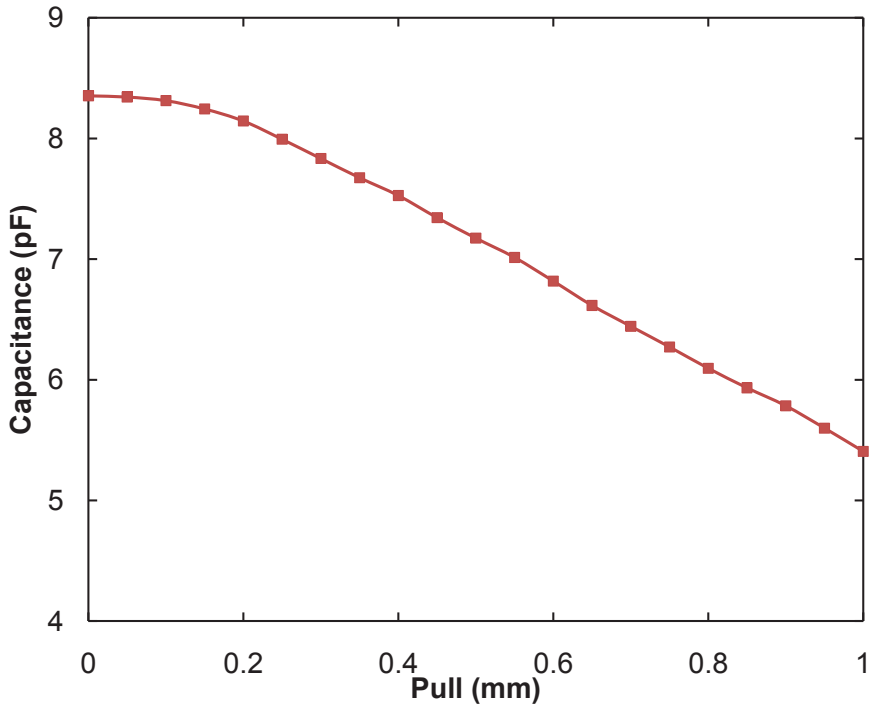

Figure 5.13. Capacitance vs. pull variation using linear tensile test when the IDC was stretched from 0 to 1mm.

5.6.3 Finite Element Analysis of Variable IDC

A finite element analysis was performed to optimize the dimensions of the PDMS encapsulation. For this analysis the Kapton and thin metal film were not considered since PDMS is the dominating mechanical factor that decides the reaction to the applied force. Figure 5.14 shows the finite element analysis model for variable IDC. For a PDMS encapulation size of 11.92mm (long) by 11.49mm (wide) by 2.6mm (thick), a linear pull of 1mm results in a force of approximately 5N as shown in Fig. 5.15. These finite element analysis results were experimentally verified using force analysis as described in the following section.

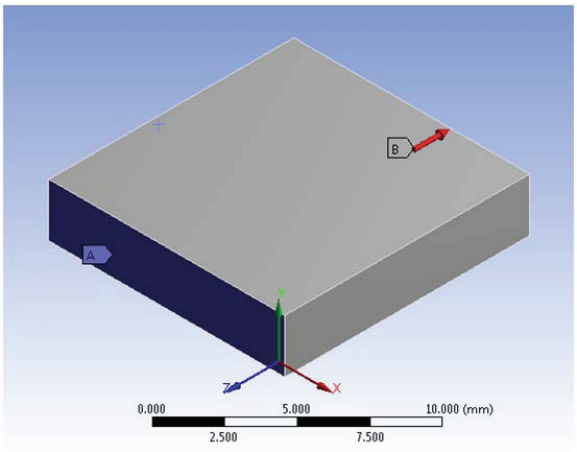

Figure 5.14. Finite element analysis setup for force characterization of variable interdigitated capacitor.

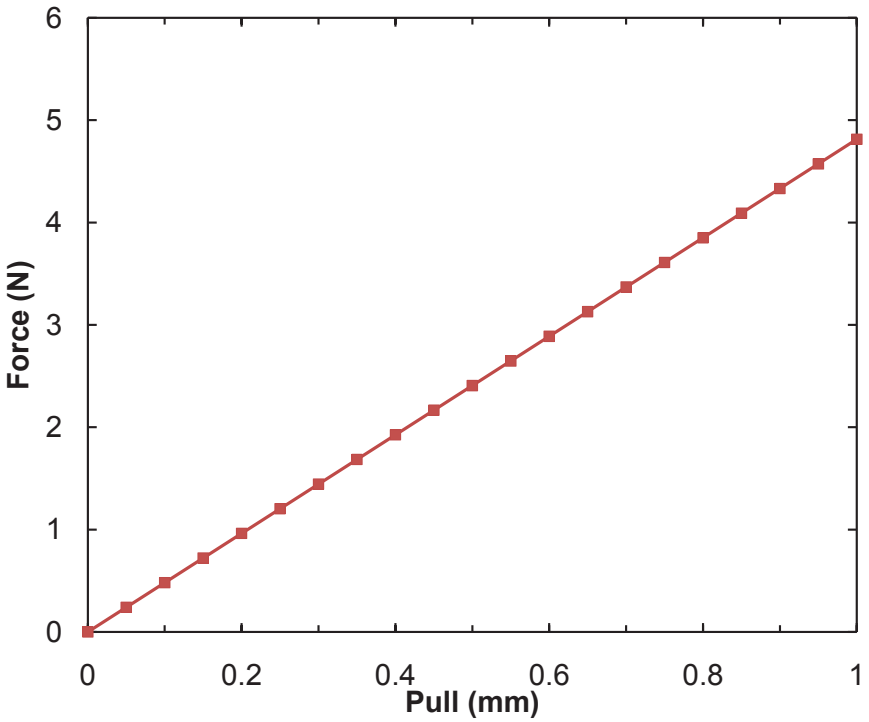

Figure 5.15. Finite element analysis results showing force vs. pull distribution for variable IDC.

5.6.4 Experimental Verification of FEA by Force Characterization

The results of the finite element analysis were experimentally verified using a force characterization setup as shown in Fig. 5.16. Here, the fixed end of the variable IDC was connected to a commercial piezoresistive force sensor which measures the force that was generated due to linear pull by the micrometer. As the micrometer was gradually increased from 0 to 1mm, the resulting force on the piezoresistive sensor increased to approximately 5N (as shown in Fig. 5.17). This matched closely with the finite element analysis from the previous section. Thus, we can see that the variable IDC fabricated using the flexible biocompatible material PDMS can be used as a force sensor. For the variable IDC to be integrated in a wireless sensing system, the mechanical parameter (force/pressure) should be converted to an equivalent electrical parameter (capacitance). The change in capacitance causes a change in the frequency of the wireless system which can be detected. Thus, the change in pressure can be measured as an equivalent change in frequency. The characterization steps to realize this system are presented in the following section.

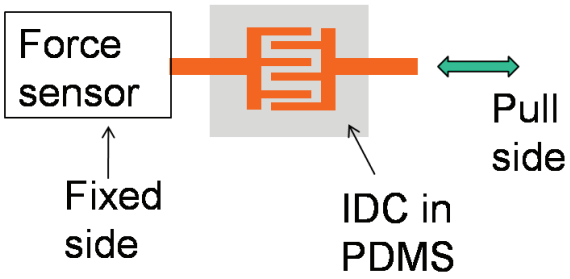

Figure 5.16. Experimental setup for force vs. pull characterization.

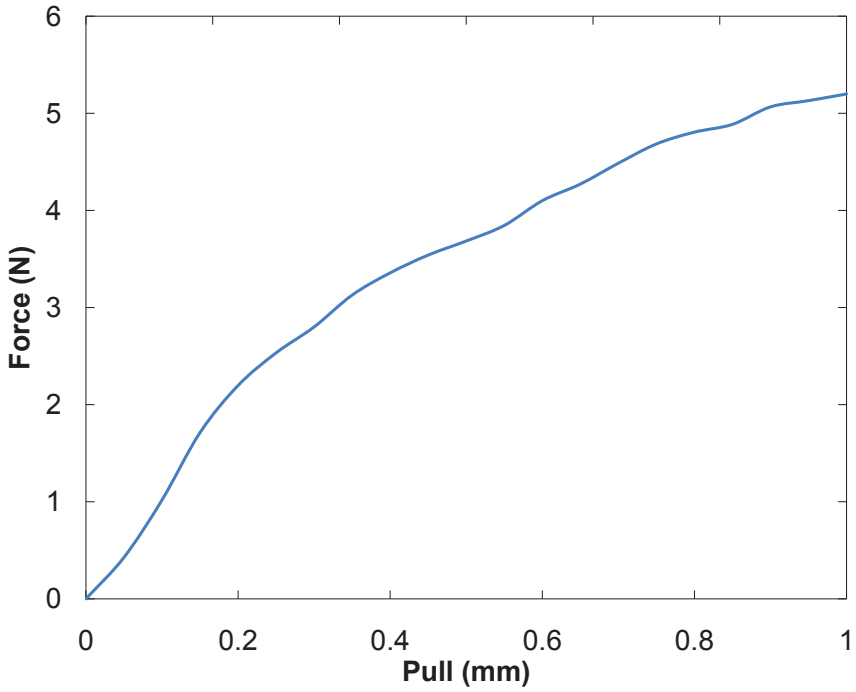

Figure 5.17. Experimental results of force vs. pull distribution for variable IDC.

5.6.5 Capacitance vs. Force Characterization

In order to measure capacitance for any force, capacitance versus force characterization was performed using the setup shown in Fig 5.18. In this setup, the fixed end of the variable IDC was connected to a commercial piezoresistive force sensor which measures the force that was generated due to linear pull by the micrometer which was connectd to the free end. An Agilent 4192A impedance analyzer measures the instantaneous capacitance of the variable IDC due to this applied force. As the force was increased from 0N to 5N (in steps of 0.5N), the capacitance of the variable IDC decreased by 2.5pF as shown in Fig. 5.19. In order to be integrated with a wireless system, this capacitance change should be converted to frequency change so that the sensor information can be wirelessly transmitted over a carrier signal. In our wireless pressure sensing system based on the variable IDC, we propose to use a

relaxation oscillator design to convert the capacitance change due to force/pressure variatioin into frequency change as presented in the following section.

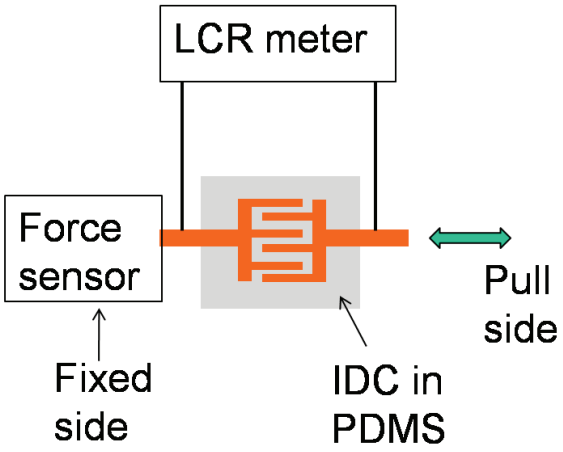

Figure 5.18. Experimental setup for capacitance vs. force characterization.

5.7 Capacitance vs. Frequency Characterization

A relaxation oscillator is an oscillator in which a capacitor is charged gradually and then discharged rapidly. A relaxation oscillator is basically an astable multivibrator, that is, it is an electronic circuit that operates between two quasi-stable states namely, "ON" and "OFF" at a certain frequency. A relaxation oscillator using a comparator circuit is shown Fig. 5.20. This oscillator generates an output frequency based on the RC time constant in the circuit [77]. The resistors R_1, R_2 and R_3 are chosen so that output frequency is a square wave which can help in unique capacitance detection at the receiver of the wireless system. When the variable IDC capacitance C changes due to the applied force, the resulting output square wave frequency also changes. Figure 5.21 shows the experimental setup in which a commerical piezoresistive force sensor was connected to the fixed end. The free end was clamped to a

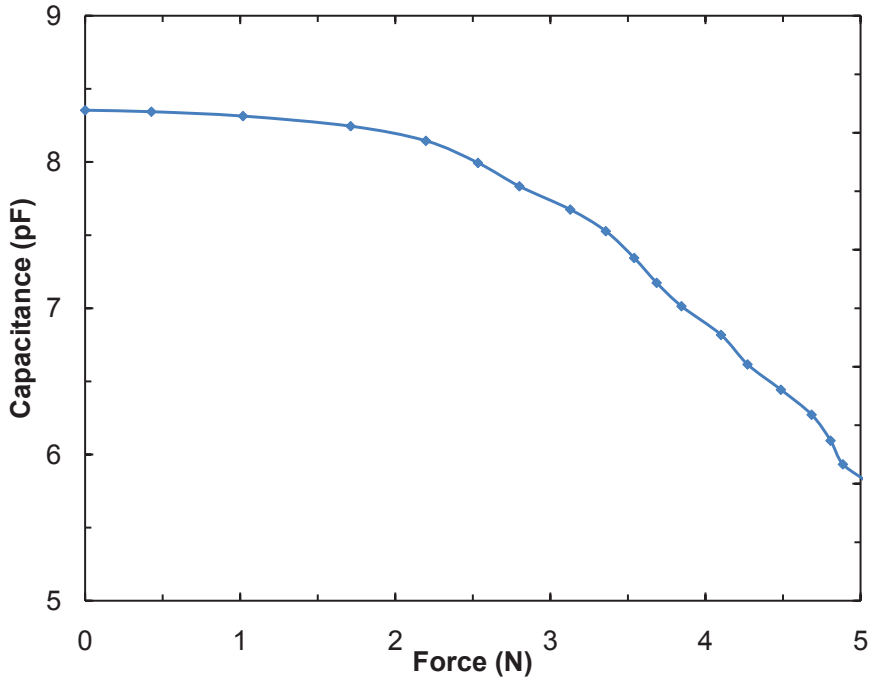

Figure 5.19. Experimental results of capacitance vs. force characterization.

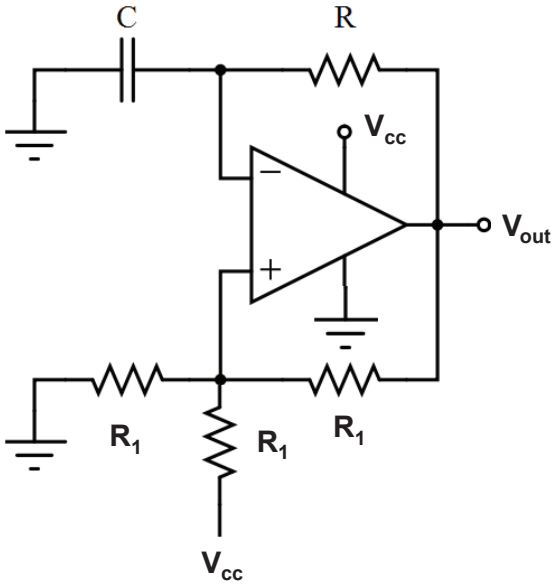

Figure 5.20. Schematic showing relaxation oscillator circuit for capacitance to frequency conversion.

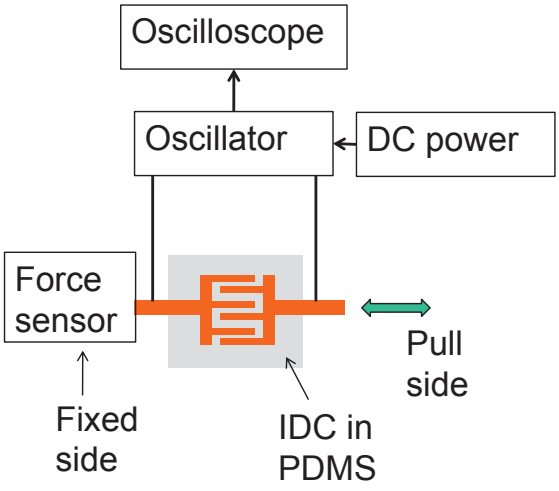

Figure 5.21. Experimental setup for frequency vs. pull characterization of variable IDC employing PDMS encapsulation.

micrometer controlled stage which can stretch the varible IDC along one axis. The variable IDC was now a part of the relaxation oscillation circuit. When there was no pull, the oscillating frequency was about 40.16kHz. At 2mm pull, the oscillating frequency increased to 43.06kHz since the capacitance decreases with pull. These results are shown in Fig. 5.22. The desired operating frequency (less than 20kHz) can be achieved easily by connecting a fixed capacitor in parallel with the variable IDC. Thus, we have shown that a variable IDC can be used to induce a frequency

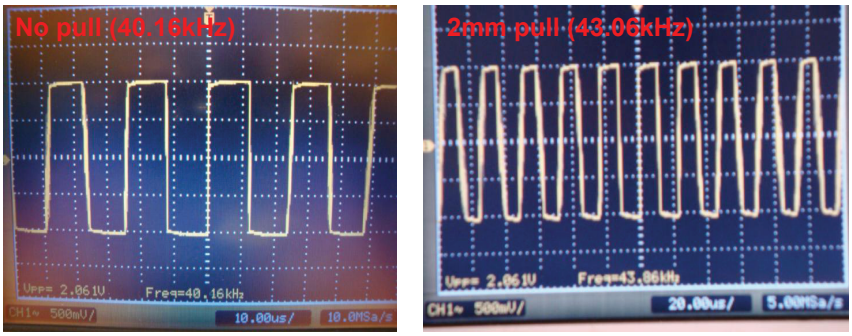

Figure 5.22. Experimental results showing the variation of frequency with linear pull of (a) 0mm and (b) 2mm.

change in a relaxation oscillator circuit due to the external pressure change sensed by the IDC.

5.8 Summary

An interdigitated capacitor (IDC) was fabricated on a biocompatible planar Kapton film. Kapton, being flexible and having very good mechanical and thermal resistance, is essential to keep the IDC finger structures intact. These IDCs were encapsulated with a biocompatible polymer, Polydimethylsiloxane (PDMS) to make the IDC variable. PDMS maintains very good elastic properties while being resistant to most chemicals and maintains structural integrity even after repeated mechanical stretching cycles. The simple fabrication process for making the variable IDC has potential for mass production, thereby reducing cost. The property that the instantaneous capacitance of the variable IDC is directly proportional to the overlapped length and inversely proportional to gap between the fingers, can be used in detecting pull, force, or pressure changes. To integrate with a wireless system, the variable IDC was subjected to various electro mechanical analysis.

Capacitance characterization using linear tensile test showed that the capacitance of the IDC for a given pull distance remained constant even after repeated cycles. As the pull increased gradually, the IDC capacitance decreased since the un-overlapped finger length increased. A finite element analysis (FEA) was used to analyze the force on the IDC due to applied linear pull. Experimental results using a commercial piezoelectric force sensor showed that the force experienced by the variable IDC matched with FEA indicating that the finite element analysis can be used to optimize the device dimensions required for a specific application. Additionally, the force experienced by the IDC can be well controlled. Capacitance characterization using force analysis gave the information about the IDC behavior under a known force

which was essential for the IDC to be used for pressure measurements. In order to implement the full potential of using variable IDC for wireless pressure measurements, the capacitance to frequency conversion was done using a relaxation oscillator. Relaxation oscillator generates a square wave based on the instantaneous capacitance of the variable IDC. Integration of this relaxation oscillator system containing variable IDC into our passive wireless system capable of pressure sensing will be discussed in chapter 6.

CHAPTER 6

WIRELESS PRESSURE SENSOR FOR GI MANOMETRY

6.1 Motivation

Medical electronics in health care plays a very significant role in overcoming many problems in diagnosis and treatment. Wireless solutions are preferred since wires are often bulky, unsafe, uncomfortable or even impossible to be deployed in some circumstances. Wireless communication devices can be categorized into two groups, active and passive. In active devices, the power source is a battery. These devices have a limited life time and are usually bulky. In the case of passive devices, the power required for operation of the sensing system is harvested from external or internal sources. Passive devices can be very small and can be used over longer periods eliminating the need for invasive procedures for replacement of batteries or sensors. In passive wireless devices, once the sensing system is implanted, diagnostic or therapeutic data can be collected on-demand. Currently there are no means to monitor the conditions of an esophageal stent after implantation. Our proposed design uses a passive wireless pressure sensing system for esophageal manometry using a variable IDC as the sensing element. The pressure exerted on the stent by the tumors in the esophagus cause a change in the capacitance of the variable IDC that can be monitored wirelessly.

6.2 Wireless System Design

Figure 6.1 shows the schematic of the wireless system. It has two main parts: the reader and the sensor. The reader is general purpose RFID reader modified to read

the frequency-varying signal [78]. The front end of the reader has a coil antenna (of size 12cm × 15cm) which was made from an AWG26 magnetic wire wound around a foam board resulting in an inductance of 17μH with a quality factor of approximately 70. This antenna coupled with coupling capacitors forms an LC resonator with center frequency of 1.34MHz. The resonator helps in transmitting the high power carrier from a class E amplifier to the sensor side and in coupling back the carrier signal that has been modulated by the sensor back to the reader. A class E power amplifier was chosen due to its high efficiency and has been employed in transcutaneous power transfer in wireless systems [79–81]. When the modulated signal is transmitted from the sensor side to the reader side over the wireless link, the voltage level at the reader coil fluctuates. This signal is extracted by the envelope detector and fed through the bandpass filter to extract the signal and suppress the high frequency carrier. This required signal representing the instantaneous capacitance of the variable IDC was then amplified and analyzed on a spectrum analyzer.

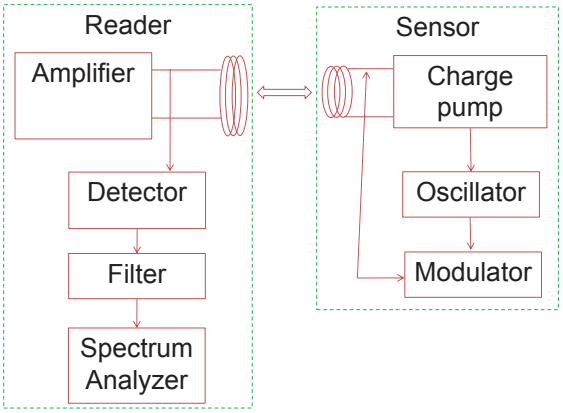

Figure 6.1. Schematic of the proposed wireless system showing the functional blocks connected through RF wireless channel.

The front end of the sensor is a coil antenna (22μH made with AWG34 magnetic wire) and a capacitor (680pF) forming a resonant circuit to receive power from the reader and send modulated data back. The power is inductively coupled between the reader antenna and the sensor antenna. The inductively coupled voltage decreases inversely as cube of the distance between the sensor and reader antennae [82]. A charge pump circuit, which is a voltage multiplier [83] and the regulator is used to build up a constant DC level to operate the rest of the circuit elements (oscillator and modulator). The relaxation oscillator (refer section 6.4) generates a square wave modulating frequency depicting the instantaneous capacitance of the variable IDC. A transistor modulator varies the carrier frequency using the frequency generated by the relaxation oscillator and couples it back to the reader side through the wireless link formed between the sensor and reader coil antennae. This wireless sensing system was integrated with an *in vitro* system that can mimic pressure variations in the esophagus.

6.3 *In vitro* System

In order to test the wireless pressure sensing system in an environment similar to the physiological conditions, an *in vitro* system was designed and built as shown in Fig. 1.2. It contains a PDMS stent (as shown in Fig. 6.3) with an internal diameter of 17mm and 10cm long and mimics a commercial esophageal stent. Esophageal pressure is in the range of 2kPa to 20kPa. In order to have a system that can operate under the previously mentioned pressure range, the thickness of the PDMS stent was obtained from finite element analysis and found to be approximately 2mm. The pressure inside the PDMS stent was simulated using a fine motion pressure valve to pass compressed dry air though a steel pipe. One end of the PDMS stent was connected to the free end of this pipe while the other end was sealed with a steel stop valve. A commercial

pressure gauge (with a range 0 to 100kPa) measured the pressure of the compressed air in the in vitro system. The variable IDC was wound around the PDMS stent to measure the radial pressure changes in the *in vitro* system. Pressure in the *in vitro* system was increased gradually and the resulting instantaneous capacitance of the variable IDC was measured using an Agilent 4192A impedance analyzer.

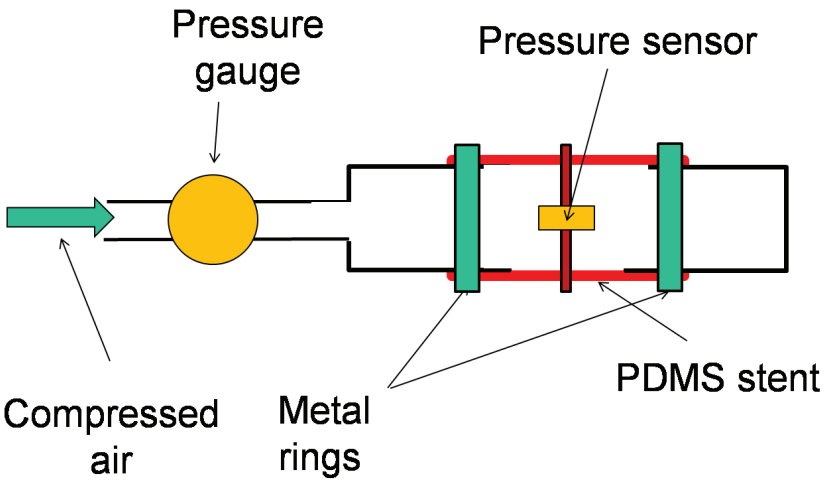

Figure 6.2. Experimental setup for in-vitro testing showing a PDMS stent integrated with wireless pressure sensor.

Figure 6.4 shows capacitance versus radial pressure distribution from the *in vitro* system. It can be seen that when the pressure was increased from 10kPa to 35kPa, the capacitance of the variable IDC decreased from 8.2pF to 5.7pF. This demonstrates the feasibility of using a variable IDC for radial pressure measurements. In order to demonstrate wireless feasibility for pressure measurement, the variable IDC was integrated with the wireless pressure sensing system described in section 6.2. With a pressure increase of approximately 25kPa, the frequency due to change in the capacitance of the variable IDC decreased by approximately 3.5kHz as shown in Fig. 6.4. Thus, we have demonstrated that a variable IDC fabricated using a flexible biocom-

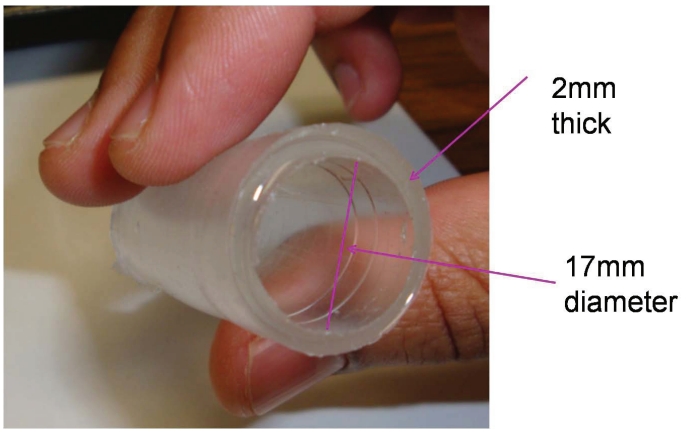

Figure 6.3. Image showing a biocompatible stent fabricated using PDMS for *in vitro* analysis of variable IDC.

patible material can be integrated with a passive wireless system and has a potential for esophageal manometry. The variable IDC can also measure changes in the axial direction. In order to use the variable IDC for axial pressure measurements, the axial strain analysis was performed as described in the following section.

6.4 Axial Pressure Sensing

As mentioned earlier, the variable IDC can be used as an axial pressure sensor. In order to implement this functionality, we need to characterize the device capacitance as a function of the applied strain. Towards this end, a strain sensing setup was designed and built using a rectangular cantilever and the variable IDC on PDMS. By knowing the material properties of the beam and applying a known weight at the free end of the cantilever, the resulting strain at any point on the beam can be determined as described in the following section.

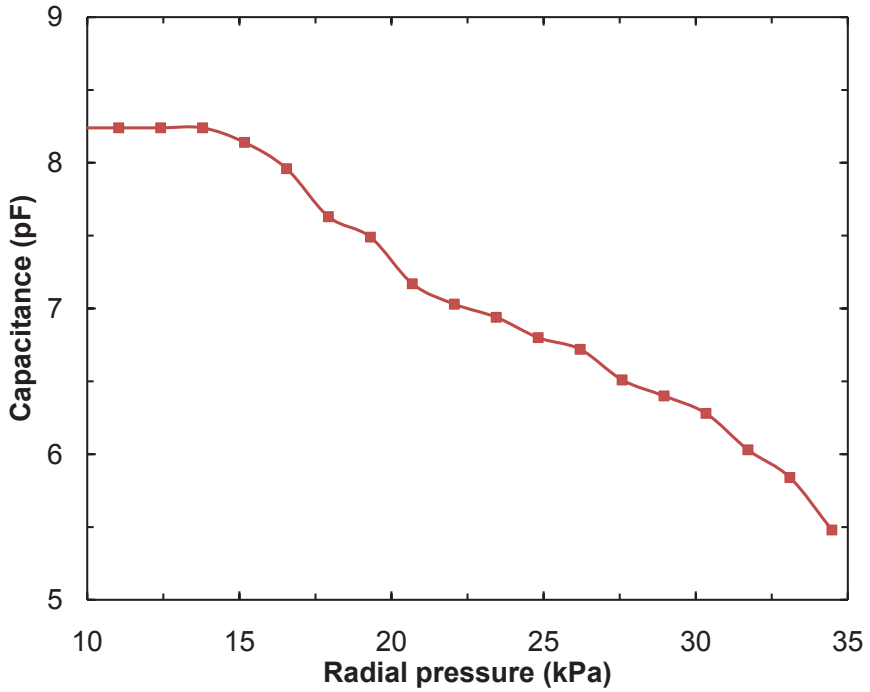

Figure 6.4. Experiment results showing capacitance vs. radial pressure distribution using *in vitro* setup when the pressure was increased from 10kPa to 35kPa.

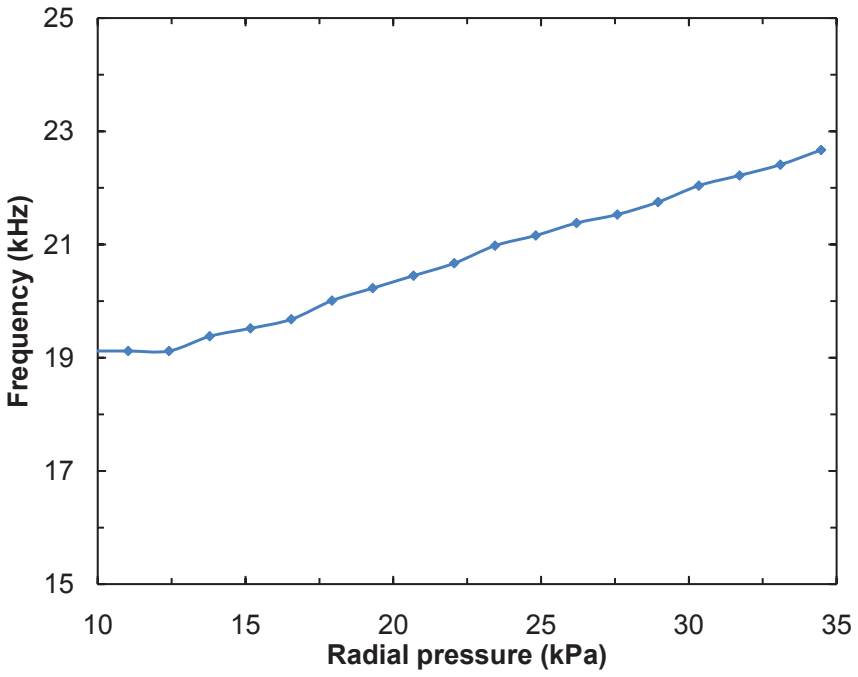

Figure 6.5. Experiment results showing frequency vs. radial pressure distribution using integrated wireless system and *in vitro* setup.

6.4.1 Strain Sensing System

A cantilever is a beam fixed at one end. A cantilever whose properties are known can be used in the measurement of strain on a device by mounting it and subjecting the beam to loads leading to axial strains. We have used a rectangular aluminum beam as the cantilever material. Figure 6.6 shows a variable IDC mounted on a rectangular aluminum cantilever.

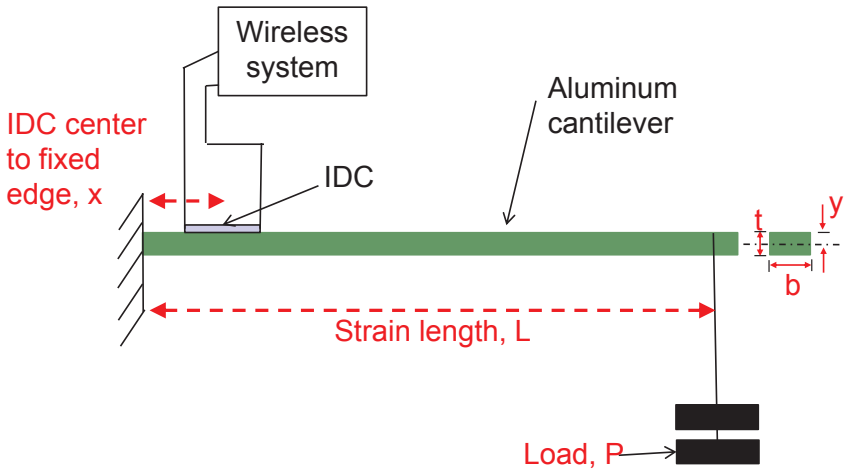

Figure 6.6. Schematic showing the experimental setup for strain analysis.

When a load P is applied on the free end of the cantilever (dimension L × b × t), it generates a moment M at the location of the variable IDC given by [84],

$$M = -P(L - x)$$

By the elastic flexure formula, the stress experienced by the variable IDC can be written as [85],

$$\sigma = \frac{-yM}{I}$$

where y is the distance from the neutral axis of the cantilever to the variable IDC and is equal to $t/2$. The moment of inertia for a rectangular cantilever beam is given by [86, 87],

$$I = \frac{bt^3}{12}$$

Substituting the equations for stress, y and moment of inertia in the moment equation, we get

$$\sigma = \frac{[-P(L-x)]\,\frac{t}{2}}{\frac{bt^3}{12}}$$

or

$$\sigma = \frac{6P(L-x)}{bt^2}$$

By Hooke's law, the stress σ is directly proportional to the strain ε_x and is given by,

$$\sigma = E\varepsilon_x$$

where E is the elastic modulus. Comparing the previous two equations, we get

$$\varepsilon_x = \frac{6P(L-x)}{Ebt^2}$$

Thus, we can determine the strain at a given point x from the fixed edge of the cantilever. For a given cantilever (with known dimensions and material properties), the strain at a point is directly proportional to the applied load. By applying a known load, desired strain can be induced in the required region of the cantilever. Strain induced on an aluminum cantilever (L=9in, b=0.5in and t=0.25in) at a distance of 0.5mm from the fixed end, when subjected to loads between 0 and 30lbs are calculated and tabulated in table 6.1. A variable IDC attached on the cantilever in this region experiences the same strain as the cantilever. Thus, by analyzing the strain behavior,

the strain on the variable can be determined. The characterization of the strain behavior of the variable IDC is discussed in the following section.

Table 6.1. Strain variation of cantilever beam with respect to applied load

Weight (lbs)	**Strain (%)**
0	0
5	0.35
10	0.71
15	1.06
20	1.41
25	1.77
30	2.12

6.4.2 Strain Characterization of Variable IDC

Figure 6.6 shows the experimental setup for strain characterization. It shows a rectangular aluminum cantilever mounted with variable IDC. The IDC is integrated with the wireless system as described in section 6.2. By gradually increasing the load from 0 to 30lbs (in steps of 5lbs), a tensile strain of 0 to 2.12% (in steps of 0.35%) is generated at a point 0.5in from the fixed end. This variation is tabulated in table 6.1. The variation of frequency in the wireless system resulting from this strain is shown in Fig. 6.7. It can be seen that when the strain increases by 2.12%, the resulting output frequency of the wireless system decreases by 4.23kHz (from 10.27kHz to 6.04kHz). Thus, we have demonstrated that the variable IDC can be used to measure the radial pressure as well as the axial strain in an integrated passive wireless sensing system using biocompatible materials. If the variable IDC can be fabricated using biodegrable materials, the device can pass through the digestive system after its desired functions are accomplished. This will create a self disposable pressure sensor which does not

require any invasive procedures to remove the sensor once it has been implanted. A wireless sensing system employing variable IDC fabricated using biodegradable polymer, Poly(1,8-Octanediol-co-Citrate) (POC) is dicussed in the following section.

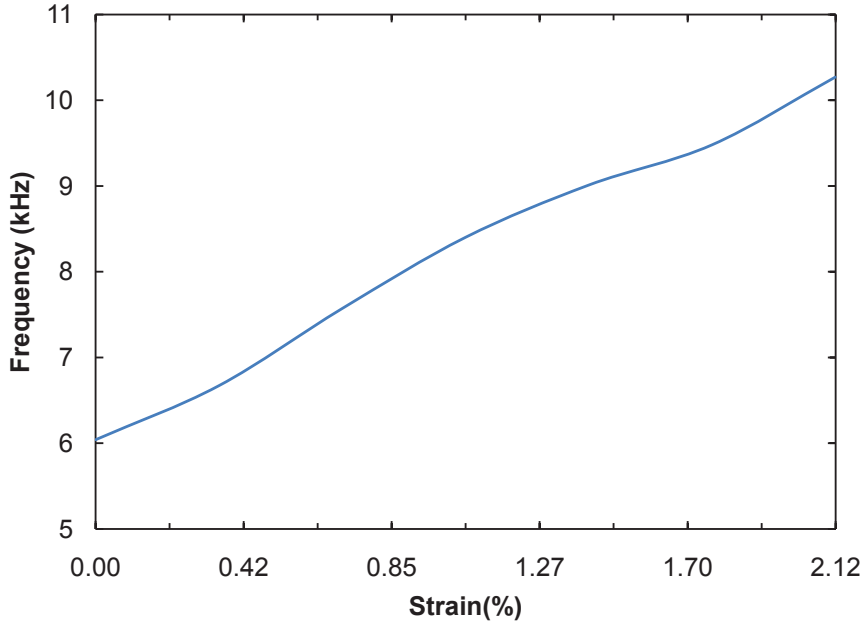

Figure 6.7. Frequency vs. strain characterization when the strain is increased from 0 to 2.12%.

6.5 Biodegradable Polymer, POC

Poly(diol citrates) are a family of biodegradable and elastomeric polyesters which are synthesized by the reaction of citric acid with various diols to form a covalent cross-linked network via a polycondensation reaction without using exogenous catalysts [88, 89]. POC is a poly(diol citrates) polymer in which the composition of prepolymer is approximately 1:1 (citric acid:1,8-octanediol). Synthesis of POC is simple and is conducted under easily manageable conditions using commercially available

chemicals from Sigma-Aldrich. Equimolar amounts of citric acid and 1,8-octanediol were added to a 250 ml three-neck round bottom flask fitted with an inlet and outlet adapter. The mixture was melted at 160 to 165^{o}C under a flow of nitrogen gas while stirring. The temperature of the system was subsequently lowered to 140^{o}C for 30min under stirring to create a pre-polymer. The pre-polymer was postpolymerized at 80^{o}C for 4 days for cross-linking. The synthesized POC is a strong elastomeric and biodegradable material with tensile elongation more than 367%, tensile strength more than 11.15MPa and Young's modulus of approximately 1.85 which makes it a good candidate for use with a variable IDC. A new fabrication technique was developed to implement variable IDC using POC biodegradable polymer.

6.5.1 Fabrication of Variable IDC Employing POC Polymer

A new fabrication process was developed to fabricate a variable IDC on Kapton using POC biodegradable polymer for encapsulation. The fabrication steps are summarized in table 6.2. A clean 135μm thick kapton film is laser machined using Oxford lasers E-355-3-OA system as described in chapter 5. The IDCs have a constant IDC line gap and line widths of 35μm and 40μm respectively. To eliminate the de-tethering steps in the previous fabrication processes, a spring design was made on the left and right side of the IDC as shown in Fig. 6.8. This also compensated for the very high elastomeric property of the POC polymer. The machined IDCs were solvent cleaned and blown dry to remove any laser debris attached to the device. A thin metal film of 0.4μm thick copper was deposited using evaporation.

The POC prepolymer being a very thick viscous fluid is mixed with dioxane solvent in the ratio of 30% pre-polymer and 70% solvent by weight to make it less gelatinous for ease of handling. This mixture was stirred using a magnetic stirrer for about 45min to get a very uniform polymer solution which was easier for pouring.

Table 6.2. Fabrication of variable IDC using biodegradable POC polymer

Step	Process
1	Laser machining of IDC structure on Kapton
2	Solvent clean and blow dry to remove laser etched debris
3	Evaporate thin-film
4	Synthesize POC prepolymer
5	Mix POC prepolymer and dioxane solvent
6	Stir solution to get uniform polymer solution
7	Pour mixed polymer solution in IDC encapsulation setup
8	Degas setup in vacuum chamber to remove entrapped air in the polymer solution
9	Dioxane solvent evaporation at room temperature in an exhaust hood
10	Cure polymer in oven at 80degC

A single step encapsulation by POC was required to get a uniform cross-linking of the polymer throughout the IDC. Hence, a new curing setup was built as shown in Fig. 6.9. It consists of a teflon petri dish in which teflon spacers were used to elevate the IDC strucure so that there was encapsulation on all sides of the device. Two teflon solid tubes are used to hold the IDC structure in place from the top and also to isolate the IDC soldering pads from encapsulation. Teflon was chosen because of its inertness with POC biodegradable polymer and also due to high temperature stability during the curing process. The POC-dioxane solution was now poured in the IDC curing setup. A vacuum pump was used to degas any entrapped air in IDC finger region. The setup with polymer solution was kept in an exhaust hood for 24hrs to evaporate the dioxane solvent. This leaves behind only POC prepolymer encapsulation of the IDC. The setup was transferred to an oven (80^oC for 4 days) for curing and crosslinking so that the cured POC encapsulated IDC can be easily peeled-of from the teflon petri dish. Figure 6.10 shows a POC encapsulated IDC

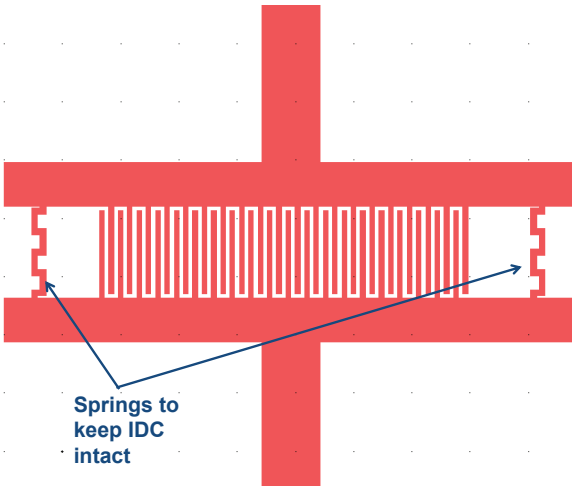

Figure 6.8. Schematic of interdigitated capacitor with spring design created using Tanner L-Edit.

with 80 fingers 1.5mm long. Characterization of biodegrable polymer based IDC is discussed in the following section.

6.5.2 Characterization of POC polymer encapsulated IDC

In order to demonstrate the feasibility of using the variable IDC employing POC biodegradable polymer for pressure sensing applications, the following characterization were performed on the 80 fingers (L=1.5mm) IDC:

1. A linear pull test to determine the capacitance under tensile loading
2. A frequency versus pull test to determine feasibility in a integrated wireless system

The experimental setup for the linear pull test is shown in Fig. 6.11 in which one end of the IDC was fixed using a clamping fixture. The free end was clamped to a micrometer controlled stage which can stretch the varible IDC in one direction. AWG 34 magnetic wires were soldered to the two exposed electrodes of the variable IDC and connected to an Agilent 4192A impedance analyzer for measuring the instantaneous

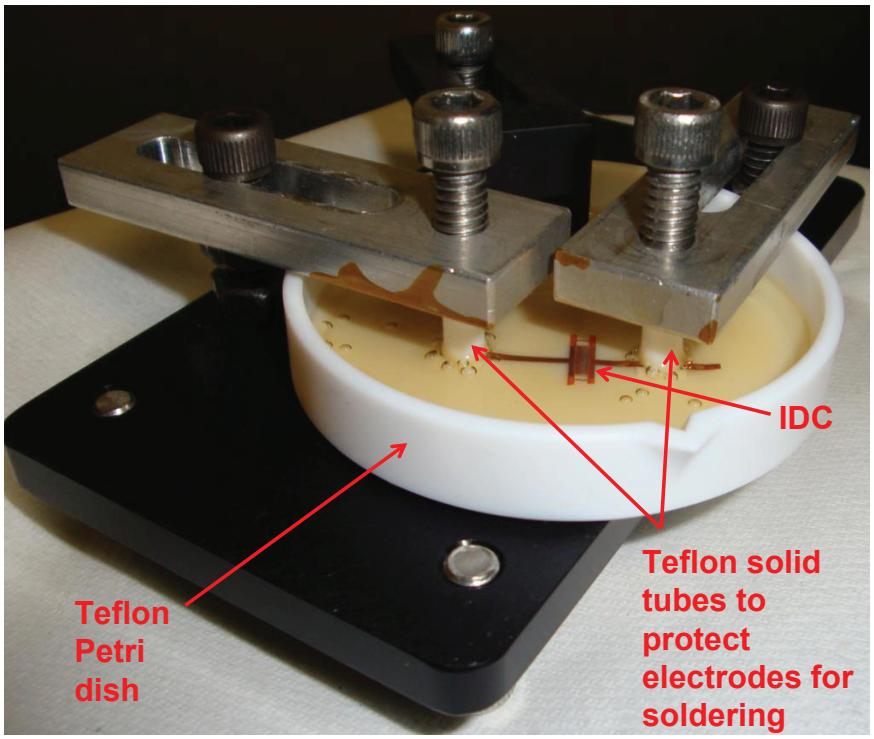

Figure 6.9. Image showing the curing setup for single step POC biodegradable encapsulation of IDC.

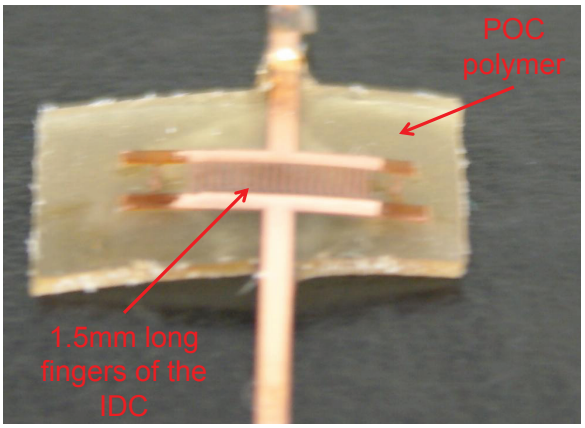

Figure 6.10. Image showing a 80 fingers 1.5mm long variable IDC employing POC biodegradable polymer encapsulation.

capacitance. The micrometer was rotated clockwise in steps of 0.25mm to stretch the variable IDC and the resulting capacitance was measured. Figure 6.12 shows the resulting capacitance variation due to linear pull. It can be clearly seen that as the pull distance increased from 0 to 2mm, the capacitance of the variable IDC decreased from 6.82pF to 5.17pF. These results were consistent even with repeated experimental cycles. The variable IDC on a biocompatible polymer was then integrated with a wireless system and tested.

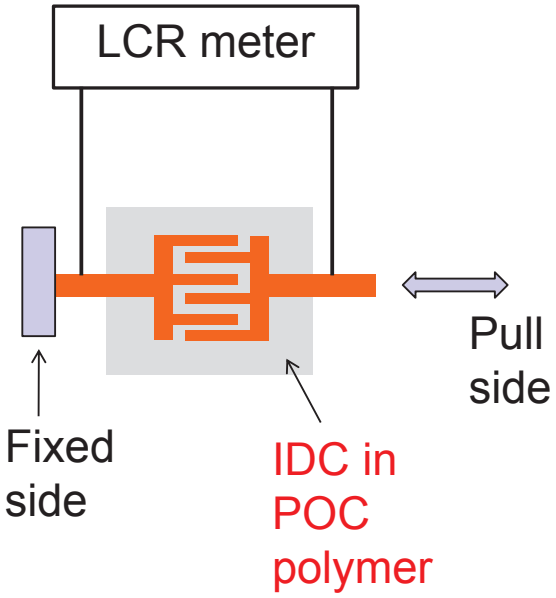

Figure 6.11. Schematic showing the experimental setup for capacitance versus pull characterization of POC polymer encapsulated IDC.

The variable IDC of the linear pull setup was integrated as part of relaxation oscillator system as shown in Fig. 6.13. Similar to the linear tensile setup, one end of the IDC was fixed using a clamping fixture. The free end was clamped to a micrometer controlled stage which can stretch the varible IDC in one direction. AWG 34 magnetic wires were soldered to the two exposed electrodes of the variable

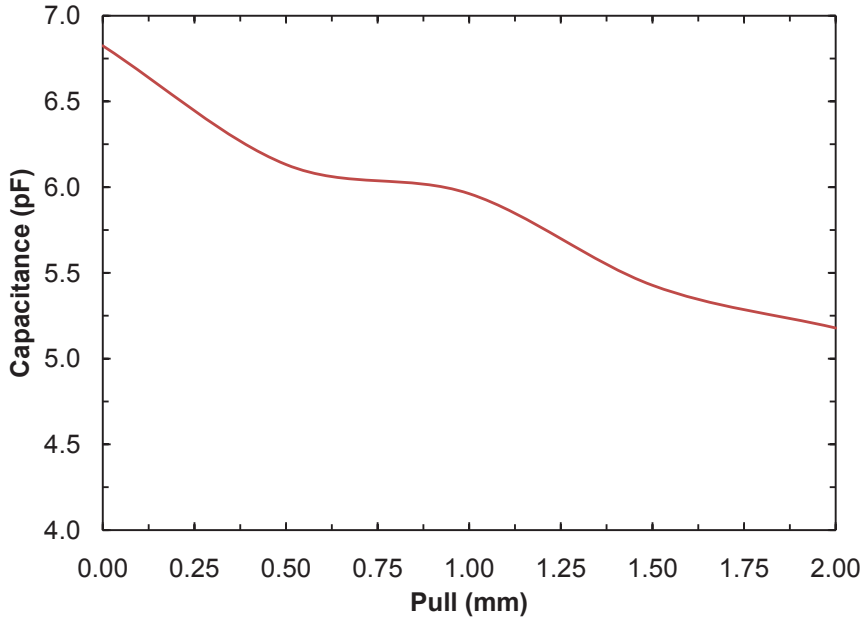

Figure 6.12. Capaciatance vs. pull characterization results for the variable IDC employing POC biodegradable polymer.

IDC as before and connected to the oscillator circuit of the passive wireless sensing system. The micrometer was rotated clockwise gradually in steps 0.25mm to stretch the variable IDC and the resulting frequency of the wireless system was analyzed on the spectrum analyzer. Figure 6.14 shows the resulting frequency variation due to the linear pull. It shows that, when the pull distance increased from 0 to 2mm, the sensor frequency of the wireless system decreased by 3.4kHz indicating that the capacitance changed in response to the pull. Thus, we have designed, tested and fabricated a variable IDC employing POC biodegradable polymer.

6.6 Summary

A wireless batteryless pressure sensor for esophageal manometry that has potential for long term monitoring, has been demonstrated. The sensor employing biocompatible materials can be easily configured to measure either radial pressure

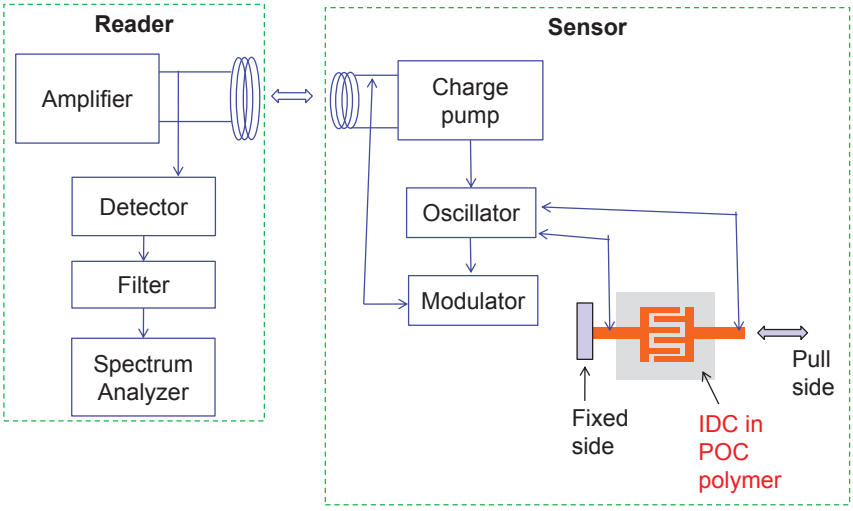

Figure 6.13. Schematic showing the experimental setup for capacitance versus characterization of POC polymer encapsulated IDC.

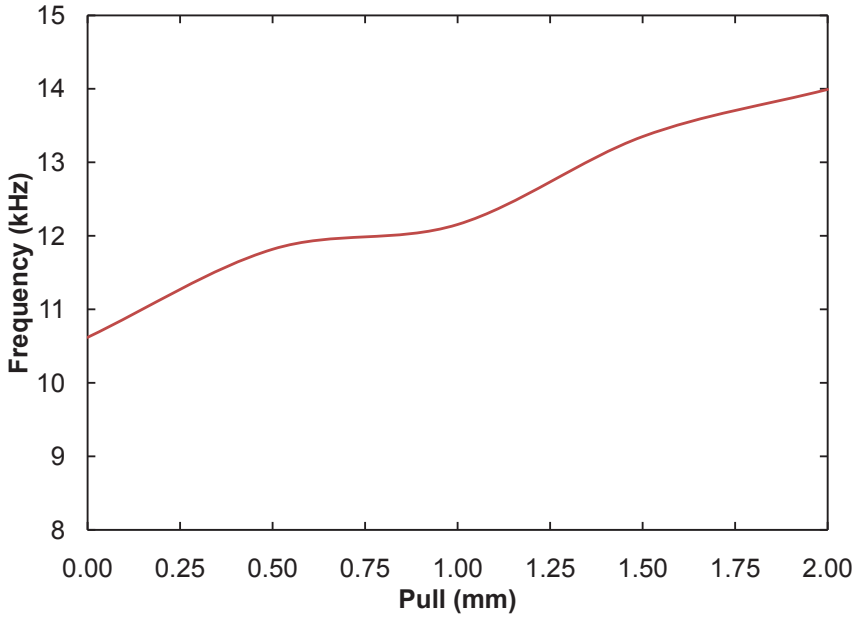

Figure 6.14. Frequency vs. pull characterization results for the variable IDC employing POC biodegradable polymer.

or axial pressure variations. An *invitro* setup was designed using PDMS stent to demonstrate feasibility for radial pressure measurement. The capacitance of the IDC decreased by 2.5pF when the pressure was increased by 25kPa implying a sensitivity of 0.1pf/kPa. In the integrated wireless system, the sensitivity as determined using the *invitro* system was 0.14kHz/kPa.

We have also designed, fabricated and tested a variable IDC employing poly(1,8-octanediol-co-citrate) (POC) biodegradable polymer which was our goal. A miniature device employing biodegradable material will dissolve and pass through the digestive system eliminating the need to remove the implanted device by invasive surgery. The final device will have gold as the electrode to make it biocompatible. The thin film disintegrates and passes through the body once the biodegradable POC polymer dissolves. Initial feasibility analysis shows that the biodegradable polymer encapsulated IDC can be potentially used in wireless gastrointestinal manometry applications.

CHAPTER 7

FUTURE WORK

7.1 Discussion

In this dissertation, two novel devices for biomedical applications have been investigated. The first device was an imaging system based on spectral optical coherence tomography (OCT) and the second was a wireless pressure system for esophageal manometry.

The proposed miniature spectral OCT scanner which employs external electromagnetic actuation can be made very small since there are no physical electrical connections to the system. Conventional imaging systems use bulky optics and cannot be miniaturized. Fiber optic based imaging systems are light and compact.

The proposed wireless pressure sensing system uses a planar interdigitated capacitor (IDC) as the pressure sensing element. The IDC was fabricated on a flexible substrate making it easy to integrate with commercial esophageal stents due to its compliant design.

The fabrication of the cantilever based system for spectral OCT used a simple fabrication process. The fiber optic based imaging system reduced the overall size of the scanner. The dimensions of the fabricated scanner were 70mm (long) $\times$ 2mm (wide) $\times$ 3.19mm (thick). The rectangular cantilever employed showed very good linearity and stability which are important requirements for OCT imaging. In our system design, an optical assembly was mounted on a ferromagnetic gel coated cantilever and steered with an external electromagnet. The experimental results closely matched the simulation results obtained from the finite element analysis. An optical

modulation efficiency of 87% for optical coherent tomography using a superluminescent diode laser at 780nm with power of 2mW and a FWHM bandwidth of 49nm was achieved at an imaging rate of 40 frames per second and a scanning range of 1.4mm. The optimization of the scanning distance and the resonant frequency was performed using different ferromagnetic materials (nickel, cobalt and iron) and different scanner lengths (60mm, 70mm and 80mm) were also assessed. Cobalt showed the maximum scanning distance for a given cantilever length. The 80mm long cantilever design had the highest scanning distance for a given ferromagnetic material. Thus, a cobalt based scanner with a cantilever length of 80mm would be ideal for large scanning distances.

In the second part, the design, fabrication and testing of a wireless pressure system for esophageal manometry was presented. The proposed approach was based on capacitance measurement using a variable interdigitated capacitor that can detect separately both the radial and axial pressure. The variable IDC was characterized using various tests: frequency sweep analysis, linear pull tests, force characterization and finite element analysis. The frequency detection approach used in the wireless system had better performance of longer read range and more reliable data that was independent of the reading position. An *in vitro* system was designed and built to show the feasibility of using the proposed pressure sensor. The device can be used for long term monitoring of esophageal pressure. The design methodology of this wireless batteryless sensor could be easily adapted to any other resistive, capacitive or voltage based sensors that can be deployed in other monitoring needs in medicine. The sensor was also fabricated on a biodegradable material. By controlling the properties of the polymer, its degradation inside the body can be predetermined. Thus, the sensor can be tailored for specific monitoring durations.

7.2 Limitations

There were some limitations encountered with the devices. One of the problems encountered during imaging using the miniature spectral OCT scanner was that the spectrometer CCD needed to be triggered at the right time for proper recording of the image parameters. This trigger was to be synchronized with the scanning of the cantilever in order to reduce imaging errors and to record all scanned data. In order to use the triggering signal from the AC source to trigger the CCD line camera, the delay between the AC source and the scanner motion should also be incorporated. The delay between the time when the AC signal was applied and the scanner actually moves was 11.98 ms. The trigger signal from the AC source itself had a delay of 25.6ms. So a total delay of 37.58ms was added to the trigger signal just before the signal was fed to the CCD trigger port.

Some problems were also encountered during the fabrication of variable IDC employing biodegradable POC polymer. One limiting factor was the curing/cross-linking time of 4 days required for the polymer which may be a factor in mass production. The IDC on the POC polymer needed a single step encapsulation to get a uniform polymerization throughout the device. During the curing process, the dioxane solvent which was used to reduce viscosity of the POC polymer starts evaporating. The amount of evaporation needs to be carefully controlled. Thus the conditions used should be very carefully controlled and should be repeatable. Hence the dioxane-to-POC polymer ratio must be constant in order to get repeatable dimensions of POC encapsulation around the IDC structure.

7.3 Future Work

For the miniature spectral OCT system, the future work needs to focus on packaging the scanner and testing for *in vivo* feasibility. Every scan with current imaging scanner leads to a two- dimensional image showing the depth information along a single scan line. With multiple fiber assemblies on a single ferromagnetic coated cantilever, a three dimensional image (showing depth in a given area) can be imaged in a single scan. Long term reliability studies on the scanner are also important.

For the wireless, batteryless pressure sensing system employing biocompatible materials, there is a need to test the system *in vivo*. For the biodegradable polymer based IDC, the next step should be to perform the degradation analysis and to optimize the designed lifetime of the device by controlling the dimensions and cross-linking of the POC biodegradable polymer. The wireless system sensor circuitry needs to be migrated on to VLSI chips to realize the full potential of miniaturization. We have conducted some preliminary strain analysis using the variable IDC which shows that other potential applications include structural health monitoring.

APPENDIX A

LASER MACHINING PROGRAM FOR IDC FABRICATION

```
;THIS PROGRAM CUTS A IDC with fingers more than 40 and length more than 1.5mm

DVAR $PASSES
DVAR $XSTART, $YSTART, $ZSTART
DVAR $NXSTART, $NYSTART, $NZSTART
DVAR $FINGERSET
DVAR $SIDEX, $SIDEY
DVAR $FASTMOVE, $SPEED
DVAR $COUNTER
DVAR $DISTX
DVAR $XBIG $XSMALL
DVAR $XLEFT
DVAR $XRIGHT
DVAR $YBIG $YSMALL
DVAR $CHECK $CUTIDC $CUTPLUS

.*****************************************************************************
;
;G108
$DO0.X=0
G91
G71   ;ALL UNITS ARE IN MM.  SPEED IS IN MM/S
.*****************************************************************************
;
MSGBOX (DF_MSGBOX_OKONLY + DF_ICON_QUESTION), "This cuts a IDC from absolute
XYZ position.  Are both the Safety and Laser Shutter Open? Please Open Now"
$XSTART=MSGINPUT DF_MSGBOX_OKONLY "X-START FOCAL POSITION; Enter Absolute X-
Pos for starting focal scan, in mm;"
$YSTART=MSGINPUT DF_MSGBOX_OKONLY "Y-START FOCAL POSITION; Enter Absolute Y-
Pos for starting focal scan, in mm;"
$ZSTART=MSGINPUT DF_MSGBOX_OKONLY "Z-START FOCAL POSITION; Enter Absolute Z-
Pos for starting focal scan, in mm;"
$FINGERSET=MSGINPUT DF_MSGBOX_OKONLY "Finger sets; Enter Number of finger sets
greater than 40;"
$PASSES=MSGINPUT DF_MSGBOX_OKONLY "Passes; Enter Number of passes;"
$SIDEY=MSGINPUT DF_MSGBOX_OKONLY "IDC Length; Enter length of IDC, in mm;"
$SIDEX=0.08
;********** CHANGE THE FOLLOWING TO 0.5 FOR DEFAULT CUT SPEED
$SPEED=0.5

MSGDISPLAY 1, "Absolute X = ", $XSTART
MSGDISPLAY 1, "Absolute Y = ", $YSTART
```

```
MSGDISPLAY 1, "Absolute Z = ", $ZSTART
MSGDISPLAY 1, "Fingerset = ", $FINGERSET
MSGDISPLAY 1, "Passes = ", $PASSES
MSGDISPLAY 1, "IDC Length = ", $SIDEY
MSGDISPLAY 1, "Cut SpeeD = ", $SPEED
;MSGDISPLAY 1, "XTEMP = ", $XTEMP
;MSGDISPLAY 1, "YTEMP = ", $YTEMP
;MSGDISPLAY 1, "XSMALL = ", $XSMALL
;MSGDISPLAY 1, "YSMALL = ", $YSMALL
;MSGDISPLAY 1, "XBIG = ", $XBIG
;MSGDISPLAY 1, "YBIG = ", $YBIG
;MSGDISPLAY 1, "NXSTART = ", $NXSTART
;MSGDISPLAY 1, "NYSTART = ", $NYSTART
;MSGDISPLAY 1, "NZSTART = ", $NZSTART

$FASTMOVE=10

;*************************************************************************
;
;************* START IDC cut
;logic to check if IDC cut is needed
$CHECK=0
$CHECK=MSGINPUT DF_MSGBOX_OKONLY "IDC Cut; Do you want IDC cut (2=YES, 0=NO);"
IF ($CHECK < 1)
;               If the answer is NO, it will still cut once to get the XLEFT and XRIGHT values
                $CUTIDC=1
ELSE
                $CUTIDC=$PASSES
ENDIF
;END logic to check if IDC cut is needed
G109
;***********following two lines get the position to initial X,Y,Z position
G90 G1 X$XSTART Y$YSTART  F30
G90 G1 Z$ZSTART F5
G91
G4 F0.25
$DO0.X=1
; outer loop for number of passes
RPT $CUTIDC
                $DO0.X=1
                G108
```

```
            G91
            G1 Y$SIDEY F$SPEED
            G1 X-$SIDEY F$SPEED
            G1 Y-$SIDEY F$SPEED
            $XLEFT=$STATUS[_PositionCnts].X/10000
            MSGDISPLAY 1, "XLEFT = ", $XLEFT
            G1 X$SIDEY F$SPEED
            ; inner loop for number of finger sets
            RPT $FINGERSET
                        G1 X$SIDEX F$SPEED
                        G1 Y$SIDEY F$SPEED
                        G1 X$SIDEX F$SPEED
                        G1 Y-$SIDEY F$SPEED
            ENDRPT
            ; END inner loop for number of finger sets
            G1 X$SIDEY F$SPEED
            $XRIGHT=$STATUS[_PositionCnts].X/10000
            MSGDISPLAY 1, "XRIGHT = ", $XRIGHT
            G1 Y$SIDEY F$SPEED
            G1 X-$SIDEY F$SPEED
            G109
            $DO0.X=0
; END outer loop for number of passes
G90 G1 X$XSTART Y$YSTART  F30
G90 G1 Z$ZSTART F5
ENDRPT
;************* END IDC cut
;*************************** This part is to cut outside CROSS region of IDC for electrode

; GOES TO INITIAL POSITION OF OUTER CROSS
$NXSTART=$XLEFT-1
$NYSTART=$YSTART-0.5
$NZSTART=$ZSTART
MSGDISPLAY 1, "NXSTART = ", $NXSTART
MSGDISPLAY 1, "NYSTART = ", $NYSTART
MSGDISPLAY 1, "NZSTART = ", $NZSTART
$XSMALL=2
$YSMALL=$SIDEY+1
$XBIG=($XRIGHT+1-$NXSTART-$XSMALL)/2
$YBIG=10
```

```
MSGDISPLAY 1, "XSMALL = ", $XSMALL
MSGDISPLAY 1, "YSMALL = ", $YSMALL
MSGDISPLAY 1, "XBIG = ", $XBIG
MSGDISPLAY 1, "YBIG = ", $YBIG

G90 G1 X$NXSTART Y$NYSTART F30
G90 G1 Z$NZSTART F5
G91
G4 F0.25
;logic to check if PLUS cut is needed
$CHECK=0
$CHECK=MSGINPUT DF_MSGBOX_OKONLY "Cut Cross; Do you want cut CROSS (2=YES,
0=NO);"
IF ($CHECK < 1)
        $CUTPLUS=1
ELSE
        $CUTPLUS=$PASSES
ENDIF
;END logic to check if PLUS cut is needed
$DO0.X=1
; loop to cut CROSS
RPT $CUTPLUS
        G108
        G91
        G1 Y$YSMALL F$SPEED
        G1 X$XBIG F$SPEED
        G1 Y$YBIG F$SPEED
        G1 X$XSMALL F$SPEED
        G1 Y-$YBIG F$SPEED
        G1 X$XBIG F$SPEED
        G1 Y-$YSMALL F$SPEED
        G1 X-$XBIG F$SPEED
        G1 Y-$YBIG F$SPEED
        G1 X-$XSMALL F$SPEED
        G1 Y$YBIG F$SPEED
        G1 X-$XBIG F$SPEED
        G109
ENDRPT
;END loop to cut CROSS
$DO0.X=0
```

```
G90 G1 X$XSTART Y$YSTART  F30
G90 G1 Z$ZSTART F5
G91
$DO0.X=0
G4 F0.1
G4 F0.01
M2
```

REFERENCES

[1] D. Jiles, *Introduction to magnetism and magnetic materials.* Chapman and Hall, 1991.

[2] P. C. Phuyal, "Fiber optic scanner using electromagnetic actuation with different ferromagnetic materials," Master's thesis, The University of Texas at Arlington, 2006.

[3] P. Dario, M. C. Carrozza, A. Benvenuto, and A. Menciassi, "Micro-systems in biomedical applications," *Journal of Micromechanics and Microengineering*, vol. 10, no. 2, pp. 235–244, 2000. [Online]. Available: http://stacks.iop.org/0960-1317/10/235

[4] S. S. Saliterman, *Fundamentals of bioMEMS and medical microdevices.* Wiley-Interscience ; Bellingham, Wash. : SPIE Press, c2006., 2006.

[5] Y. HAGA and M. ESASHI, "Biomedical microsystems for minimally invasive diagnosis and treatment," *Proceedings of the IEEE*, vol. 92, no. 1, pp. 98–114, Jan 2004.

[6] K. J. REBELLO, "Applications of mems in surgery," *Proc. IEEE*, vol. 92, no. 1, pp. 43–55, Jan. 2004.

[7] K. Gilleo, "Mems in medicine," *Circuits Assembly*, vol. 16, no. 8, pp. 32 – 33, 2005.

[8] P. C. Enzinger and R. J. Mayer, "Esophageal cancer," *N Engl J Med*, vol. 349, no. 23, pp. 2241–2252, 2003. [Online]. Available: http://content.nejm.org

[9] S. Law and J. Wong, "Current management of esophageal cancer," *Journal of Gastrointestinal Surgery*, vol. 9, no. 2, pp. 291–310, Feb. 2005. [Online]. Available: http://dx.doi.org/10.1016/j.gassur.2004.06.007

[10] A. F. Fercher, W. Drexler, C. K. Hitzenberger, and T. Lasser, "Optical coherence tomography - principles and applications," *Reports on Progress in Physics*, vol. 66, no. 2, pp. 239–303, 2003. [Online]. Available: http://stacks.iop.org/0034-4885/66/239

[11] D. Huang, E. Swanson, C. Lin, J. Schuman, W. Stinson, W. Chang, M. Hee, T. Flotte, K. Gregory, C. Puliafito, and a. et, "Optical coherence tomography," *Science*, vol. 254, no. 5035, pp. 1178–1181, 1991. [Online]. Available: http://www.sciencemag.org/cgi/content/abstract/254/5035/1178

[12] B. E. Bouma and G. J. Tearney, *Handbook of Optical Coherence Tomography*. Informa Healthcare, 2001.

[13] P. H. Tomlins and R. K. Wang, "Theory, developments and applications of optical coherence tomography," *Journal of Physics D: Applied Physics*, vol. 38, no. 15, pp. 2519–2535, 2005. [Online]. Available: http://stacks.iop.org/0022-3727/38/2519

[14] J. Schmitt, "Optical coherence tomography (oct): a review," *Selected Topics in Quantum Electronics, IEEE Journal of*, vol. 5, no. 4, pp. 1205–1215, Jul/Aug 1999.

[15] M. Lee, J. Izatt, E. Swanson, D. Huang, J. Schumun, C. Lin, C. Puliafito, and J. Fujimoto, "Optical coherence tomography for ophthalmic imaging: new technique delivers micron-scale resolution," *Engineering in Medicine and Biology Magazine, IEEE*, vol. 14, no. 1, pp. 67–76, Jan/Feb 1995.

[16] M. Kankaria, "Design and construction of a fast spectrometer for fourier domain optical coherence tomography," Master's thesis, The University of Texas at Arlington, May 2006.

[17] J. F. Arevalo, Ed., *Retinal Angiography and Optical Coherence Tomography*. Springer, 2008.

[18] N. Nassif, B. Cense, B. Park, M. Pierce, S. Yun, B. Bouma, G. Tearney, T. Chen, and J. de Boer, "In vivo high-resolution video-rate spectral-domain optical coherence tomography of the human retina and optic nerve," *Opt. Express*, vol. 12, no. 3, pp. 367–376, 2004. [Online]. Available: http://www.opticsexpress.org/abstract.cfm?URI=oe-12-3-367

[19] S. Yun, G. Tearney, B. Bouma, B. Park, and J. de Boer, "High-speed spectral-domain optical coherence tomography at 1.3 μm wavelength," *Opt. Express*, vol. 11, no. 26, pp. 3598–3604, 2003. [Online]. Available: http://www.opticsexpress.org/abstract.cfm?URI=oe-11-26-3598

[20] A. Rollins, S. Yazdanfar, M. Kulkarni, R. Ung-Arunyawee, and J. Izatt, "In vivo video rate optical coherence tomography," *Opt. Express*, vol. 3, no. 6, pp. 219–229, 1998. [Online]. Available: http://www.opticsexpress.org/abstract.cfm?URI=oe-3-6-219

[21] W. Drexler, U. Morgner, F. X. Kärtner, C. Pitris, S. A. Boppart, X. D. Li, E. P. Ippen, and J. G. Fujimoto, "In vivo ultrahigh-resolution optical coherence tomography," *Opt. Lett.*, vol. 24, no. 17, pp. 1221–1223, 1999. [Online]. Available: http://ol.osa.org/abstract.cfm?URI=ol-24-17-1221

[22] A. Sergeev, V. Gelikonov, G. Gelikonov, F. Feldchtein, R. Kuranov, N. Gladkova, N. Shakhova, L. Snopova, A. Shakhov, I. Kuznetzova, A. Denisenko, V. Pochinko, Y. Chumakov, and O. Streltzova, "In vivo endoscopic oct imaging of precancerand cancer states of human mucosa,"

Opt. Express, vol. 1, no. 13, pp. 432–440, 1997. [Online]. Available: http://www.opticsexpress.org/abstract.cfm?URI=oe-1-13-432

[23] K. Kobayashi, J. A. Izatt, M. D. Kulkarni, J. Willis, M. V. Sivak, and Jr., "High-resolution cross-sectional imaging of the gastrointestinal tract using optical coherence tomography: preliminary results, ,," *Gastrointestinal Endoscopy*, vol. 47, no. 6, pp. 515 – 523, 1998. [Online]. Available: http://www.sciencedirect.com/science/article/B6WFY-4HJYPYH-F/2/05fcd0abd6859a5eb1fee8ae57548be2

[24] M. Wojtkowski, R. Leitgeb, A. Kowalczyk, T. Bajraszewski, and A. F. Fercher, "In vivo human retinal imaging by fourier domain optical coherence tomography," *Journal of Biomedical Optics*, vol. 7, no. 3, pp. 457–463, 2002. [Online]. Available: http://link.aip.org/link/?JBO/7/457/1

[25] S. P. Fang and H. F. Taylor, "High-performance single-mode fiber-optic switch," *Opt. Lett.*, vol. 19, no. 16, pp. 1204–1206, 1994. [Online]. Available: http://ol.osa.org/abstract.cfm?URI=ol-19-16-1204

[26] S.-S. Lee, E. Motamedi, and M. C. Wu, "Surface-micromachined free-space fiber optic switches with integrated microactuators for optical fiber communication systems," in *Proc. International Conference on Solid State Sensors and Actuators TRANSDUCERS '97 Chicago*, vol. 1, 1997, pp. 85–88.

[27] I. R. Matas, M. Lpez-Amo, F. Montero, C. Fernndez-Valdivielso, F. J. Arregui, and C. Bariin, "Low-cost optical amplitude modulator based on a tapered single-mode optical fiber," *Appl Opt*, vol. 40, no. 2, pp. 228–234, Jan 2001.

[28] S. A. Boppart, B. E. Bouma, C. Pitris, G. J. Tearney, J. G. Fujimoto, and M. E. Brezinski, "Forward-imaging instruments for optical coherence tomography." *Opt Lett*, vol. 22, no. 21, pp. 1618–1620, Nov 1997.

[29] R. W. Nelson, J. R. Krone, and O. Jansson, "Surface plasmon resonance biomolecular interaction analysis mass spectrometry. 1. chip-based analysis," *Analytical Chemistry*, vol. 69, no. 21, pp. 4363–4368, Nov. 1997. [Online]. Available: http://dx.doi.org/10.1021/ac970538w

[30] M. Sedlar, V. Matejec, and I. Paulicka, "Optical fibre magnetic field sensors using ceramic magnetostrictive jackets," *Sensors and Actuators A: Physical*, vol. 84, no. 3, pp. 297 – 302, 2000. [Online]. Available: http://www.sciencedirect.com/science/article/B6THG-40VT255-J/2/af03fd49da0415b5ed752151f0a8f68e

[31] R. S. Popovic, J. A. Flanagan, and P. A. Besse, "The future of magnetic sensors," *Sensors and Actuators A: Physical*, vol. 56, no. 1-2, pp. 39 – 55, 1996. [Online]. Available: http://www.sciencedirect.com/science/article/B6THG-3TTDFRM-7/2/4c488ba62c3de9847b4c93babb6e322b

[32] F. Keplinger, S. Kvasnica, A. Jachimowicz, F. Kohl, J. Steurer, and H. Hauser, "Lorentz force based magnetic field sensor with optical readout," *Sensors and Actuators A: Physical*, vol. 110, no. 1-3, pp. 112 – 118, 2004, selected Papers from Eurosensors XVI Prague, Czech Republic. [Online]. Available: http://www.sciencedirect.com/science/article/B6THG-4BHJ2YB-3/2/3c2d9e4724e7f97953142a41aa6bd29b

[33] M. Herding, F. Richardt, and P. Woias, "A novel approach to low-cost optical fiber switches," in *Proc. IEEE/LEOS International Conference on Optical MEMS*, 2003, pp. 141–142.

[34] M. Hoffmann, P. Kopka, and E. Voges, "Bistable micromechanical fiber-optic switches on silicon with thermal actuators," *Sensors and Actuators A: Physical*, vol. 78, no. 1, pp. 28 – 35, 1999. [Online].

Available: http://www.sciencedirect.com/science/article/B6THG-3Y51V1J-4/2/ffb2b7613bbf8131bfe7ea063b3953e9

[35] K. R. Cochran, L. Fan, and D. L. DeVoe, "High-power optical microswitch based on direct fiber actuation," *Sensors and Actuators A: Physical*, vol. 119, no. 2, pp. 512 – 519, 2005. [Online]. Available: http://www.sciencedirect.com/science/article/B6THG-4F1GRG4-2/2/59f1982d74c1132f5bc471425a4effa1

[36] S. Nagaoka, "Compact latching-type single-mode-fiber switches fabricated by a fiber-micromachining technique and their practical applications," *IEEE J. Sel. Topics Quantum Electron.*, vol. 5, no. 1, pp. 36–45, 1999.

[37] J. Bernstein, W. Taylor, J. Brazzle, C. Corcoran, G. Kirkos, J. Odhner, A. Pareek, M. Waelti, and M. Zai, "Electromagnetically actuated mirror arrays for use in 3-d optical switching applications," *Microelectromechanical Systems, Journal of*, vol. 13, no. 3, pp. 526–535, June 2004.

[38] K. H. Gilchrist, R. P. McNabb, J. A. Izatt, and S. Grego, "Piezoelectric scanning mirrors for endoscopic optical coherence tomography," *Journal of Micromechanics and Microengineering*, vol. 19, no. 9, p. 095012 (11pp), 2009. [Online]. Available: http://stacks.iop.org/0960-1317/19/095012

[39] C. Liu, T. Tsao, Y.-C. Tai, W. Liu, P. Will, and C.-M. Ho, "A micromachined permalloy magnetic actuator array for micro robotics assembly systems," in *Solid-State Sensors and Actuators, 1995 and Eurosensors IX.. Transducers '95. The 8th International Conference on*, vol. 1, Jun 1995, pp. 328–331.

[40] R. C. Hibbeler, *Mechanics of materials*. Prentice Hall, 2004.

[41] R. E. Rosensweig, *Ferrohydrodynamics*. Cambridge University Press, 1985.

[42] N. Dhaubanjar, "The design and analysis of optical scanners for optical coherence tomography," Master's thesis, The University of Texas at Arlington, 2006.

[43] J. P. D. Hartog, *Mechanical Vibrations*. Dover Publications Inc., 1985.

[44] P. Pandojirao-Sunkojirao, S. M. N. Rao, P. C. Phuyal, N. Dhaubanjar, and J. C. Chiao, "A magnetic actuator for fiber-optic applications," *International Journal of Optomechatronics*, vol. 3, no. 3, pp. 215–232, 2009. [Online]. Available: http://www.informaworld.com/10.1080/15599610903174440

[45] T. Stolarski, Y. Nakasone, and Y. Nakasone, *Engineering Analysis with ANSYS Software*. Butterworth-Heinemann, 2007.

[46] NIH, *Esophageal Disorders*. National Institutes of Health, November 2009. [Online]. Available: http://www.nlm.nih.gov/medlineplus/esophagusdisorders.html

[47] A. C. Society, Ed., *Cancer Facts and Figures 2009*. Atlanta: American Cancer Society, 2009.

[48] H. J. Stein and J.-R. Siewert, "Improved prognosis of resected esophageal cancer," *World Journal of Surgery*, vol. 28, no. 6, pp. 520–525, June 2004. [Online]. Available: http://dx.doi.org/10.1007/s00268-004-7417-1

[49] J. Park, Y. Lee, B. Kim, J.-H. Kim, J. Park, Y. Kim, S. Lee, S. Song, and J. Chung, "Long-term clinical outcomes of self-expanding metal stents for treatment of malignant gastroesophageal junction obstructions and prognostic factors for stent patency: Effects of anticancer treatments," *Digestive and Liver Disease*, vol. In Press, Corrected Proof, pp. –, 2009. [Online]. Available: http://www.sciencedirect.com/science/article/B7582-4X8BPBC-1/2/f2d46c58318150bd88a6a2dcdc2b154f

[50] K. Knyrim, H.-J. Wagner, N. Bethge, M. Keymling, and N. Vakil, "A Controlled Trial of an Expansile Metal Stent for Palliation of Esophageal Obstruction Due to Inoperable Cancer," *N Engl J Med*, vol. 329, no. 18, pp. 1302–1307, 1993. [Online]. Available: http://content.nejm.org/cgi/content/abstract/329/18/1302

[51] I. Raijman, I. Siddique, J. Ajani, and P. Lynch, "Palliation of malignant dysphagia and fistulae with coated expandable metal stents: experience with 101 patients, ,," *Gastrointestinal Endoscopy*, vol. 48, no. 2, pp. 172 – 179, 1998. [Online]. Available: http://www.sciencedirect.com/science/article/B6WFY-4HGRV9M-8/2/166418f0f8e17f3ab771348f1f6c1a87

[52] C. Zhang, J.-M. Yu, G.-P. Fan, C.-R. Shi, S.-Y. Yu, H.-P. Wang, L. Ge, and W.-X. Zhong, "The use of a retrievable self-expanding stent in treating childhood benign esophageal strictures," *Journal of Pediatric Surgery*, vol. 40, no. 3, pp. 501 – 504, 2005. [Online]. Available: http://www.sciencedirect.com/science/article/B6WKP-4FSK3V4-8/2/4182bdff0c9c2b9f01680c5230bcea96

[53] K. Takahata and Y. B. Gianchandani, "A micromachined capacitive pressure sensor using a cavity-less structure with bulk-metal/elastomer layers and its wireless telemetry application," *Sensors*, vol. 8, no. 4, pp. 2317–2330, 2008. [Online]. Available: http://www.mdpi.com/1424-8220/8/4/2317

[54] A. DeHennis and K. Wise, "A wireless microsystem for the remote sensing of pressure, temperature, and relative humidity," *Microelectromechanical Systems, Journal of*, vol. 14, no. 1, pp. 12–22, Feb. 2005.

[55] K.-H. Shin, C.-Y. Moon, T.-H. Lee, C.-H. Lim, and Y.-J. Kim, "Implantable flexible wireless pressure sensor module," in *Sensors, 2004. Proceedings of IEEE*, Oct. 2004, pp. 844–847 vol.2.

[56] M. Fonseca, J. English, M. von Arx, and M. Allen, "Wireless micromachined ceramic pressure sensor for high-temperature applications," *Microelectromechanical Systems, Journal of*, vol. 11, no. 4, pp. 337–343, Aug 2002.

[57] H.-L. Chau and K. Wise, "An ultraminiature solid-state pressure sensor for a cardiovascular catheter," *Electron Devices, IEEE Transactions on*, vol. 35, no. 12, pp. 2355–2362, Dec 1988.

[58] W. Ko and Q. Wang, "Touch mode capacitive pressure sensors for industrial applications," in *Micro Electro Mechanical Systems, 1997. MEMS '97, Proceedings, IEEE., Tenth Annual International Workshop on*, Jan 1997, pp. 284–289.

[59] A. Chavan and K. Wise, "Batch-processed vacuum-sealed capacitive pressure sensors," *Microelectromechanical Systems, Journal of*, vol. 10, no. 4, pp. 580–588, Dec 2001.

[60] B. Gogoi and C. Mastrangelo, "A low-voltage force-balanced pressure sensor with hermetically sealed servomechanism," in *Micro Electro Mechanical Systems, 1999. MEMS '99. Twelfth IEEE International Conference on*, Jan 1999, pp. 493–498.

[61] W. Tang, T.-C. Nguyen, and R. Howe, "Laterally driven polysilicon resonant microstructures," in *Micro Electro Mechanical Systems, 1989, Proceedings, An Investigation of Micro Structures, Sensors, Actuators, Machines and Robots. IEEE*, Feb 1989, pp. 53–59.

[62] J. J. Sniegowski and E. J. Garcia, "Microfabricated actuators and their application to optics," *Micro-Optics/Micromechanics and Laser Scanning and Shaping*, vol. 2383, no. 1, pp. 46–64, 1995. [Online]. Available: http://link.aip.org/link/?PSI/2383/46/1

[63] V. K. Varadan, K. J. Vinoy, and K. A. Jose, *RF MEMS and Their Applications*. Wiley, 2002.

[64] H. J. D. L. Santos, *Introduction to Microelectromechanical Microwave Systems*. Artech House Publishers, 2004.

[65] W. M. van Spengen and T. H. Oosterkamp, "A sensitive electronic capacitance measurement system to measure the comb drive motion of surface micromachined mems devices," *Journal of Micromechanics and Microengineering*, vol. 17, no. 4, pp. 828–834, 2007. [Online]. Available: http://stacks.iop.org/0960-1317/17/828

[66] A.-Q. Liu, *Photonic MEMS devices : design, fabrication and control*. Boca Raton, FL : CRC Press, 2009.

[67] S. Gevorgian, T. Martinsson, P. Linner, and E. Kollberg, "Cad models for multilayered substrate interdigital capacitors," *Microwave Theory and Techniques, IEEE Transactions on*, vol. 44, no. 6, pp. 896–904, Jun 1996.

[68] W. Olthuis, W. Streekstra, and P. Bergveld, "Theoretical and experimental determination of cell constants of planar-interdigitated electrolyte conductivity sensors," *Sensors and Actuators B: Chemical*, vol. 24, no. 1-3, pp. 252 – 256, 1995. [Online]. Available: http://www.sciencedirect.com/science/article/B6THH-46T75DP-1T/2/6cf4c86564a12efeec7e0c89a91e3dd9

[69] H.-W. You and J.-H. Koh, "Ag(ta,nb)o3 thin-film interdigital capacitors for microwave applications," *Microelectronics Journal*, vol. 38, no. 2, pp. 222 – 226, 2007, 2005 Workshop on Thermal Investigations of ICs and Systems (THERMINIC). [Online]. Available: http://www.sciencedirect.com/science/article/B6V44-4MV1FG3-2/2/b4fe28af6a83aad7678e768cec360852

[70] H. Yoon, K. J. Vinoy, and V. K. Varadan, "Design and development of micromachined bilateral interdigital coplanar waveguide rf phase shifter compatible with lateral double diffused metal oxide semiconductor voltage controller on silicon," *Smart Materials and Structures*, vol. 12, no. 5, pp. 769–775, 2003. [Online]. Available: http://stacks.iop.org/0964-1726/12/769

[71] H.-D. Wu, Z. Zhang, F. Barnes, C. Jackson, A. Kain, and J. Cuchiaro, "Voltage tunable capacitors using high temperature superconductors and ferroelectrics," *Applied Superconductivity, IEEE Transactions on*, vol. 4, no. 3, pp. 156–160, Sep 1994.

[72] G. Alley, "Interdigital capacitors and their application to lumped-element microwave integrated circuits," *Microwave Theory and Techniques, IEEE Transactions on*, vol. 18, no. 12, pp. 1028–1033, Dec 1970.

[73] W. Gardiner and J. White, *Specialty Silicones as Building Blocks for Organic Polymer Modification in High Value Polymers*, A. Fawcett, Ed. Royal Society of Chemistry,Cambridge, 1990.

[74] T. Kendrick, B. Parbhoo, and J. White, *Siloxane Polymers and Copolymers in The Chemistry of Organic Silicon Compounds Pt 2*, S. Patai and Z. Rappoport, Eds. John Wiley,Chichester, 1989, vol. 21.

[75] S. Clarson and J. Semlyen, Eds., *Siloxane Polymers*. Prentice Hall,New Jersey, 1993.

[76] J. C. Lotters, W. Olthuis, P. H. Veltink, and P. Bergveld, "Polydimethylsiloxane as an elastic material applied in a capacitive accelerometer," *Journal of Micromechanics and Microengineering*, vol. 6, no. 1, pp. 52–54, 1996. [Online]. Available: http://stacks.iop.org/0960-1317/6/52

[77] G. Gonzalez, *Foundations of Oscillator Circuit Design*. Artech House Publishers, 2006.

[78] T. Ativanichayaphong, "Wireless devices for medical applications," Ph.D. dissertation, The University of Texas at Arlington, 2007.

[79] P. Troyk and G. DeMichele, "Inductively-coupled power and data link for neural prostheses using a class-e oscillator and fsk modulation," in *Engineering in*

Medicine and Biology Society, 2003. Proceedings of the 25th Annual International Conference of the IEEE, vol. 4, Sept. 2003, pp. 3376–3379 Vol.4.

[80] N. Chaimanonart and D. Young, "Remote rf powering system for wireless mems strain sensors," *Sensors Journal, IEEE*, vol. 6, no. 2, pp. 484–489, April 2006.

[81] K. WISE, D. ANDERSON, J. HETKE, D. KIPKE, and K. NAJAFI, "Wireless implantable microsystems: high-density electronic interfaces to the nervous system," *Proceedings of the IEEE*, vol. 92, no. 1, pp. 76–97, Jan 2004.

[82] S. Chen and V. Thomas, "Optimization of inductive rfid technology," in *Electronics and the Environment, 2001. Proceedings of the 2001 IEEE International Symposium on*, 2001, pp. 82–87.

[83] G. De Vita and G. Iannaccone, "Design criteria for the rf section of uhf and microwave passive rfid transponders," *Microwave Theory and Techniques, IEEE Transactions on*, vol. 53, no. 9, pp. 2978–2990, Sept. 2005.

[84] F. Beer and E. Johnston, *Mechanics of Materials*. McGraw Hill, 2002.

[85] U. S. Tata, "Study of patch antennas for strain measurement," Master's thesis, The University of Texas at Arlington, 2008.

[86] Y. Jia, K. Sun, F. J. Agosto, and M. T. Quinones, "Design and characterization of a passive wireless strain sensor," *Measurement Science and Technology*, vol. 17, no. 11, pp. 2869–2876, 2006. [Online]. Available: http://stacks.iop.org/0957-0233/17/2869

[87] R. Matsuzaki and A. Todoroki, "Wireless flexible capacitive sensor based on ultra-flexible epoxy resin for strain measurement of automobile tires," *Sensors and Actuators A: Physical*, vol. 140, no. 1, pp. 32 – 42, 2007. [Online]. Available: http://www.sciencedirect.com/science/article/B6THG-4P0DJRH-1/2/27b71c0969181ec60af83016d3797f95

[88] J. Yang, A. Webb, and G. Ameer, "Novel citric acid-based biodegradable elastomers for tissue engineering," *Advanced Materials*, vol. 16, no. 6, pp. 511–516, 2004. [Online]. Available: http://dx.doi.org/10.1002/adma.200306264

[89] Y. Kang, J. Yang, S. Khan, L. Anissian, and G. A. Ameer, "A new biodegradable polyester elastomer for cartilage tissue engineering," *Journal of Biomedical Materials Research Part A*, vol. 77A, no. 2, pp. 331–339, 2006. [Online]. Available: http://dx.doi.org/10.1002/jbm.a.30607

BIOGRAPHICAL STATEMENT

Praveen Pandojirao-Sunkojirao was born in Bangalore, India, in 1978. He received his Bachelor of Engineering in Telecommunications from B. M. S College of Engineering, Bangalore University, in 2000. He received his M.S. and Ph.D. degrees from The University of Texas at Arlington in 2004 and 2009, respectively, all in Electrical Engineering. From 2000 to 2001, he was a DSP Design Engineer with RG Solutions, Bangalore, India. His current research interest is in the area of Microelectromechanical systems (MEMS), Nanofabrication, Wafer level packaging, Biomedical sensors and BioMEMS. He holds a United States patent, "Three-dimensional wafer stacking with vertical interconnects". He is a member of IEEE, SPIE, SMTA, and IMAPS societies.